Remote Sensing of Environment 263 (2021) 112564

Contents lists available at ScienceDirect

Remote Sensing of Environment

journal homepage: www.elsevier.com/locate/rse

Discrete anisotropic radiative transfer modelling of solar-induced chlorophyll fluorescence: Structural impacts in geometrically explicit vegetation canopies

Zbyněk Malenovský [a,b,*], Omar Regaieg [c], Tiangang Yin [b,d], Nicolas Lauret [c], Jordan Guilleux [c], Eric Chavanon [c], Nuria Duran [c], Růžena Janoutová [e], Antony Delavois [c], Jean Meynier [c], Ghania Medjdoub [c], Peiqi Yang [f], Christiaan van der Tol [f], Douglas Morton [b], Bruce Douglas Cook [b], Jean-Philippe Gastellu-Etchegorry [c]

[a] School of Geography, Planning, and Spatial Sciences, College of Sciences Engineering and Technology, University of Tasmania, Private Bag 76, Hobart, TAS 7001, Australia
[b] NASA Goddard Space Flight Center, Biospheric Sciences Laboratory, 8800 Greenbelt Rd, Greenbelt, MD 20771, USA
[c] Centre d'Etudes Spatiales de la Biosphère - UT3, CNES, CNRS, IRD, Université de Toulouse, 31401 Toulouse Cedex 9, France
[d] Earth System Science Interdisciplinary Center, University of Maryland, College Park, MD 20740-3823, USA
[e] Global Change Research Institute of the Czech Academy of Sciences, Bělidla 986/4a, 60300 Brno, Czech Republic
[f] Faculty of Geo-Information Science and Earth Observation (ITC), University of Twente, PO Box 217, AE Enschede 7500, the Netherlands

ARTICLE INFO

Editor name: Jing M. Chen

Keywords:
DART
Fluspect
SCOPE
SIF
Sun-/shade-adapted leaves
LAI
Clumping
Wood

ABSTRACT

Solar-induced fluorescence (SIF) is a subtle but informative optical signal of vegetation photosynthesis. Remotely sensed SIF integrates environmental, physiological and structural changes that alter photosynthesis at leaf, plant and canopy scales. Radiative transfer models are ideally suited to investigate the complex sources of variability in the SIF signal to guide the interpretation of SIF retrievals from airborne and space-borne platforms. Here, we coupled the Fluspect-Cx model of leaf optical properties and chlorophyll-*a* fluorescence with the Discrete Anisotropic Radiative Transfer (DART) model to upscale SIF from individual leaves to three-dimensional (3D) structurally explicit canopies. For one-dimensional homogeneous (turbid-like) canopies, DART-SIF was nearly identical to SIF simulated in two existing models, SCOPE and mSCOPE (RMSE <0.221 W.m^{-2}.μm^{-1}.sr^{-1}). DART simulations in geometrically explicit 3D canopies offered four important insights regarding the influence of vegetation structure on the multi-angular top-of-canopy SIF signal. First, changes in the 3D canopy architecture of maize crops, represented by leaf density (leaf area index), and plant clumping (canopy closure) had a larger impact on SIF than the modelled photosynthetic efficiency distinction between sun-adapted and shade-adapted foliage. Second, clumping of leaves at the crop and stand levels was identified as one of the key driving factors of multi-angular anisotropy of red and far-red SIF (686 and 740 nm) for both maize and eucalyptus canopies. Third, non-photosynthetic woody material had a significant impact on top-of-canopy SIF in modelled 3D forest stands. Wood shadowing decreased the photosynthetically active radiation absorbed by green leaves, and consequently the SIF emissions, by 10% in sparse and 17% in dense eucalyptus stands. The wood obstruction (blocking) effect, quantified as a relative difference of SIF escape probabilities from canopies with and without wood in the nadir viewing direction, decreased far-red SIF by 4–6% but it had a smaller and sometimes positive influence (by less than 2%) on red SIF. Fourth, DART 3D radiative budget profiles revealed that the majority of the SIF signal from a dense eucalyptus stand originated from the top 25% of the simulated canopy. Interestingly, the introduction of bark-covered woody elements did not alter the simulated balance and omnidirectional escape factor of red SIF in this upper canopy part but did raise significantly both of them in case of far-red SIF. These results demonstrate the importance of 3D radiative transfer and radiative budget simulations for investigating SIF interactions in structurally complex plant canopies and for a better understanding of spatiotemporal and multi-angular remote sensing SIF observations.

* Corresponding author at: School of Geography, Planning, and Spatial Sciences, College of Sciences Engineering and Technology, University of Tasmania, Private Bag 76, Hobart, TAS 7001, Australia.
E-mail address: zbynek.malenovsky@gmail.com (Z. Malenovský).

https://doi.org/10.1016/j.rse.2021.112564
Received 18 September 2020; Received in revised form 10 May 2021; Accepted 14 June 2021
Available online 25 June 2021
0034-4257/© 2021 Elsevier Inc. All rights reserved.

1. Introduction

The potential for airborne and spaceborne monitoring of plant productivity has motivated optical remote sensing (RS) scientists since the launch of first Earth observing satellites (Ashley and Rea, 1975; Blair and Baumgardner, 1977). The faint signal of chlorophyll *a* fluorescence has been the target of vegetation RS for several decades (Rosema et al., 1991). Although recent technological advances in narrow-band imaging spectroscopy provide the first estimates of solar-induced chlorophyll fluorescence (SIF) from space (Frankenberg et al., 2011; Guanter et al., 2007; Joiner et al., 2011), the retrieval and use of the subtle SIF signal emitted in the red and near-infrared spectral regions to assess plant productivity is fraught with natural complexity of vegetated landscapes. Hence, RS applications of SIF, including physiological principles, instruments, measurement techniques and computer models (Mohammed et al., 2019), need a further development to improve our understanding and correct interpretation of the diurnal, seasonal, and interannual variabilities in the SIF signal observed with RS instruments at local, regional and global spatial scales. In particular, SIF variability originating from multiple scattering and reabsorption within structurally complex vegetation canopies is poorly understood, as are optical interactions in topographically rough and spatially heterogeneous natural and man-made landscapes (Zhang et al., 2020).

Radiative transfer modelling is a well-established and inseparable part of modern optical RS methods (Myneni and Ross, 2012). Computer simulated radiative transfer in vegetation (Widlowski et al., 2015) has been used for local and global sensitivity analyses of various RS phenomena (e.g., Malenovský et al., 2008; Verrelst and Rivera, 2017; Verrelst et al., 2010), and also for retrieval and interpretation of quantitative vegetation descriptors from remotely sensed spectral observations obtained through various inversion procedures (e.g., Croft et al., 2020; Malenovský et al., 2013; Verrelst et al., 2019). One of the most frequently used and well-established leaf-scale RTMs is PROSPECT (Féret et al., 2021; Féret et al., 2017; Jacquemoud and Baret, 1990; Malenovský et al., 2006). Its first clone designed to simulate the chlorophyll-*a* fluorescence emission in plant leaves was FluorMODleaf (Pedrós et al., 2010), followed by computationally simpler Fluspect-B (Vilfan et al., 2016) and Fluspect-Cx (Vilfan et al., 2018). The Fluspect models reproduce leaf optical properties between 400 and 2500 nm together with 3D matrices of forward- and backward-emitted SIF per wavelength of photosynthetically active radiation (PAR) incident on the adaxial side of a dark-adapted leaf. Besides these semi-empirical models, physical 3D leaf fluorescence RTMs have been developed, e.g., the Monte Carlo (MC) Photon Transport (Sušila and Nauš, 2007) or the Fluorescence Leaf Canopy Vector Radiative Transfer model (Kallel, 2020). The MC models are, however, computationally demanding and, therefore, less suitable for an operational use in routine applications.

Models of SIF radiative transfer are developed hand-in-hand with the RS experimental work conducted at leaf as well as canopy scales (Aasen et al., 2019). Leaf RTMs are usually embedded in canopy-scale RTMs that can be classified according to the canopy representation as one-dimensional (1D) or three-dimensional (3D). Strengths and weaknesses of available canopy RTM types are reviewed in Malenovský et al. (2019). 1D models, such as SAIL (Verhoef, 1984), were designed for a horizontally homogeneous canopy with structural, optical and biochemical variability only in the vertical dimension (e.g., mono-species crops). The most frequently used SIF model for 1D canopies is a SAIL's successor called SCOPE (van der Tol et al., 2009; van der Tol et al., 2019; Yang et al., 2020a), recently extended for multi-layered canopies as mSCOPE (Yang et al., 2017). Both SCOPE models are not modelling just radiance and SIF transfer but also soil-vegetation-atmosphere temperature and energy balances, including photosynthetic processes. SCOPE is frequently used for its simplicity and robustness, but its 1D architecture is unsuitable for complex multi-species ecosystems with structurally heterogeneous canopy layers and rough topography (e.g., boreal forests or savannas; Liu et al., 2019a). Therefore, several 3D RTMs have been equipped with the ability to scale SIF from leaves to canopies to better capture the influence of structural heterogeneity of vegetation canopies. FluorWPS is a 3D MC ray-tracing SIF model (Zhao et al., 2016) that was developed and tested on 3D agricultural crops (Tong et al., 2021). Flux tracking of SIF simulated in the Discrete Anisotropic Radiative Transfer (DART) model (Gastellu-Etchegorry et al., 1996) was used to assess its multi-angular anisotropy in 3D maize canopies (Gastellu-Etchegorry et al., 2017). The Fluor-FLIGHT 3D model, developed from FLIGHT (North, 1996), supported assessment of Mediterranean oak forest water stress and *Phytophthora* infections from airborne SIF data (Hernández-Clemente et al., 2017). Finally, the FLiES MC model (Sakai et al., 2020) was used to interpret space-borne SIF of Amazonian forests (Köhler et al., 2018).

Despite the fact that all RTMs rely on simplifications and assumptions, they are powerful tools to investigate the optical interactions of SIF, which is needed for scaling and interpretation of the SIF signals acquired by proximal, airborne and spaceborne instruments (Bendig et al., 2020; Gamon et al., 2019; Wyber et al., 2017). The main goal of this paper is to demonstrate the ability of the DART model coupled with Fluspect-Cx to assess the influence of canopy 3D architecture on the top-of-canopy SIF (SIF_{TOC}) for cropland and forested environments that are difficult or even infeasible to investigate directly. DART simulations in this study address three primary research questions. First, in absence of a suitable 3D validation measurements and to verify their modelling consistency, do the DART, SCOPE and mSCOPE models provide comparable estimates of SIF_{TOC} for structurally homogenous vegetation in form of a turbid medium? Second, what is the SIF_{TOC} impact originating from biochemical leaf fluorescence efficiencies (*fqe*), varying for sun- and shade-adapted leaves, in comparison to increasing leaf density and clumping of maize (*Zea mays L.*) canopies? And third, what are the effects of woody trunks and branches on simulated SIF_{TOC}, SIF fluxes and escape factors from 3D forest abstractions of dense and sparse Australian white peppermint (*Eucalyptus pulchella*) stands?

2. Material and methods

2.1. Implementation of leaf chlorophyll fluorescence in DART

We used the 3D DART model as the pilot RTM of this study. DART, being developed by researchers from the CESBIO Laboratory in Toulouse for more than 20 years (Gastellu-Etchegorry et al., 1996), was successfully cross compared with other state-of-the-art RTMs within the RAMI exercise (Widlowski et al., 2015). It produces at-sensor top-of-atmosphere (TOA) and bottom-of-atmosphere (BOA) multi-angular RS images by tracking optical and thermal photon fluxes through any type of 3D landscape with atmosphere (Gastellu-Etchegorry et al., 2015). Additionally, it calculates the quantitative 3D radiative budget, i.e., fluxes of intercepted, absorbed, reflected and emitted radiation, in the optical spectral domain (400–2500 nm) (Gastellu-Etchegorry et al., 2004). The presence of woody material was implemented in DART in 2008 (Malenovský et al., 2008), and radiative transfer of Fluspect-Cx modelled SIF emissions in 2017 (Gastellu-Etchegorry et al., 2017). The Fluspect-Cx implementation followed the approach that was previously applied to couple DART with the PROSPECT-D model (Féret et al., 2017), taking advantage of both models' computational similarities and commonalities in input/output handling. The DART version 5.7.3, used in this work, simulates SIF radiative transfer and budget for 3D vegetation canopies constructed from geometrically explicit triangular objects (facets). Based on user-defined input parameters (i.e., leaf chlorophyll $a + b$, total carotenoid and brown pigment contents, equivalent water thickness, dry leaf mass per area, leaf mesophyll structural parameter and specific fluorescence efficiencies), Fluspect generates four SIF matrices (M_{xyij}), where x is the photosystem PSI or PSII, y is the backward or forward direction relative to radiation incident direction, i is the 1 nm excitation band in the photosynthetically active spectral region from 400 to 750 nm ($i \in [1\ I]$), and j is the 1 nm emitted

SIF band ($j \in [1\ J]$) in the spectral region from 640 to 850 nm. Consequently, the Fluspect SIF leaf exitance (F_{xyj}) at band j (1 nm bandwidth) due to irradiance (E_i) in band i is:

$$F_{xyj} = M_{xyij}.E_i \quad (1)$$

In contrast to Fluspect, DART works with any number of spectral bands that can have any bandwidth, for example with U excitation bands λ_u and V fluorescence bands λ_v. Hence, in DART, a leaf irradiance (E_u) leads to the leaf exitance:

$$F_{xyv} = M_{xyuv}.E_u \quad (2)$$

where M_{xyuv} is derived from the Fluspect matrices (M_{xyij}) using an interpolation on spectral bands ($\Delta\lambda_u = \Sigma\alpha_{ui}.\Delta\lambda_i$, $\Delta\lambda_v = \Sigma\beta_{uj}.\Delta\lambda_j$) and the two-step weighted arithmetic averaging:

$$M_{xyuv} = \frac{\sum_j \beta_{uj}.\Delta\lambda_j.M_{xyuj}}{\sum_j \beta_{uj}.\Delta\lambda_j} \quad (3)$$

$$M_{xyuj} = \frac{\sum_i \alpha_{ui}.\Delta\lambda_i.M_{xyij}}{\sum_i \alpha_{ui}.\Delta\lambda_i} \quad (4)$$

DART spectral leaf SIF exitance is accurate only if the u bands cover the entire SIF excitation spectral interval and if they do not overlap. Similarly, it simulates the whole SIF domain only if the v bands cover the whole SIF emission spectral interval.

The Fluspect calibration optical parameters (i.e., specific absorption coefficients, refractive index of mesophyll cell walls and water, etc.) are stored in an external table called Optipar. We used the Optipar table released in 2015. Additionally to the standard PROSPECT leaf biochemical and structural inputs, Fluspect requires leaf fluorescence quantum efficiencies (*fqe*), in DART referred to as fluorescence yields, for PSI and PSII. The specification of *fqe* values in DART is flexible. They can be entered per individual foliage facet or specified as general parameters that represent all leaves or a group of leaves in a given canopy. Biologically meaningful foliage groups are, for instance, sunlit (i.e., leaves exposed to direct sun radiation) and shaded leaves (i.e., leaves in the shadow of other phytoelements), or sun-adapted (i.e., leaves exposed most of the time to a direct sun radiation and subsequently adapting their pigment pools for a high photoprotective capacity) and shade-adapted leaves (i.e., leaves growing most of their lifespan under a low-intensity diffuse light and consequently having no need for a high photoprotective capacity). It is important to keep in mind that a momentarily shaded leaf can actually be sun-adapted and vice versa, depending on its instantaneous and total diurnal illumination.

The implementation of DART chlorophyll fluorescence emission F_{xyv} (Eq. 2) does not account for the microclimatic conditions influencing the actual leaf photosynthetic activity. However, F_{xyv} can be in a vertical canopy profile additionally weighted by an *eta* parameter, which adjusts the leaf SIF exitance according to actual local temperature, humidity, wind aerodynamics and other microclimatic environmental conditions. Similar to *fqe*, the *eta* profile can be inserted either for a whole canopy, per a foliage group, or per pre-defined leaf groups. Since DART modelling does not contain soil-vegetation-atmosphere transfer (SVAT) of energy, the *eta* parameter must be precomputed out of DART with a SVAT model (e.g., SCOPE; van der Tol et al., 2009) that considers dynamic meteorological factors as active parts in computation of the energy balance. DART simulates the total and the per-photosystem SIF_{TOC} radiance and TOC reflectance using the N-flux tracking transfer. Technical details about the SIF flux tracking in DART are available in the DART User's Manual (Chapter III.2.2.d; DART, 2020), while DART physical principles and mathematical descriptions are detailed in the DART Handbook (DART, 2019).

2.2. Comparison of DART and SCOPE/mSCOPE SIF radiative transfers

In absence of a suitable empirical verification data, we compared the DART SIF_{TOC} signal with comparable outcomes produced by the SCOPE model and its multi-layer extension, mSCOPE (both in version 1.62). SCOPE is a broadly accepted model that has been previously confronted and validated with SIF_{TOC} measurements of agricultural crops (van der Tol et al., 2016). It simulates vegetation canopy as a turbid medium of infinitely small leaves distributed in 60 horizontally homogeneous vertical layers (Yang et al., 2017), all of them with the same predefined leaf biochemical and canopy structural parameters. mSCOPE allows users to divide canopy into multiple horizontal layers and to assign to each one specific leaf optical properties and LAI. The methodology and graphical outputs of the DART and SCOPE/mSCOPE SIF radiative transfer comparison are, due to a large extent, provided in Appendix A.

2.3. DART modelled influence of geometrically explicit plant canopy structures on SIF

DART works with detailed and spatially explicit 3D representations of plant foliage and other canopy elements (e.g., trunks and branches), and can be, therefore, used to investigate how the structural components modulate the simulated SIF_{TOC} signal through optical photon interactions as well as via foliage shading and physiological adaptations to prevailing photosynthetic light intensity. For this purpose, we built two realistic but structurally different mono-species canopies: i) an agricultural field of 1 m tall maize plants with eight leaves, created with the open source graphical software Blender (Blender, 2007) according to a template produced by the plant architecture modelling L-system OpenAlea (Pradal et al., 2008), and ii) a 16 m tall forest stand of white peppermint trees, created from terrestrial laser scans of real trees (Janoutová et al., 2019) growing in southern Tasmania (Australia). 3D landscapes were built as juxtaposed scenes located at the same Latitude of 39.03°N and Longitude of 76.85°W (Maryland, USA) as previous simulations, with the solar angles for 10th July 2014 for the test of foliage sun and shade adaptation and for 26th August 2014 at 14.00 of local time (without the daylight saving) for tests of maize canopy clumping and eucalypt wood influence. All canopies were illuminated by the same DART-simulated BOA direct and diffuse solar irradiance, as described in the previous Section 2.2. Ground of the 3D scenes was optically defined as the Lambertian loamy gravel brown dark soil with a linearly increasing reflectance ($\rho \approx 6\%$ at 550 nm, $\rho \approx 12\%$ at 686 nm and $\rho \approx 15\%$ at 740 nm).

2.3.1. Distinction and influence of sun- and shade-adapted foliage in maize crops

As explained by Nobel (1976) or Givnish (1988), leaves growing in a shaded environment are biochemically and anatomically different from those exposed for most of the day to direct solar irradiation. DART users can consider these differences and their influence on SIF_{TOC} by classifying the facets of 3D vegetation leaves in several classes, for which leaf optical or biochemical properties (including *fqe* and *eta* parameters) can be defined separately. The final number of classes depends on the structural complexity of canopies and the availability of measurements to support the detailed foliar parameterization. A simple two-class classification would split leaf facets into just sun- and shade-adapted cohorts (DART, 2020), considering a long-term cumulative leave irradiance as the main driving force.

DART calculates intercepted, absorbed, reflected and emitted radiation, i.e. radiative budget, per 3D cell of the simulated scene and also for each surface facet in the scene (Gastellu-Etchegorry, 2008), which can be used to distinguish between the sun- and shade-adapted leaf cohorts. The intercepted radiation flux $E(\lambda)$ [$W.m^{-2}$] can be converted into photosynthetic photon flux density Q (PPFD) [$\mu mol.photons.m^{-2}.s^{-1}$] by integrating the intercepted PAR (iPAR) per leaf facet as follows:

$$Q = \int_{\Delta\lambda_i} E(\lambda)\cdot d\lambda \cdot \frac{\int_{0.4\mu m}^{0.75\mu m} L_B(T,\lambda)\cdot \frac{\lambda}{h\cdot c}\cdot \frac{10^6}{N_a}\cdot d\lambda}{\int_{0.4\mu m}^{0.75\mu m} L_B(T,\lambda)\cdot d\lambda} \quad (5)$$

where $L_B(T,\lambda)$ is Planck's law at temperature T (T = 5800 K) and wavelength λ [μm], h is Planck's constant [J.s], c is speed of light [m.s^{-1}], Na is Avogadro's constant [mole^{-1}], and $\int_{\Delta\lambda i}$ is the PAR spectral range from 400 to 750 nm. The Q value depends on the ratio of direct and diffuse irradiance spectrum, leaf optical properties and PAR multiple scattering. Influenced by literature findings about the potential of Q for differentiating sun- and shade-adapted leaves (Leuning et al., 1995; Niinemets et al., 2015), the following two classification algorithms were designed: i) a frequency double-threshold and ii) a probability distribution approach. Both methods are based on simulated leaf PAR irradiance values for T time steps during i days, with T being small enough to ensure an adequate angular sampling of leaf irradiance variation during the simulated days.

The first double-threshold approach asks user to specify high Q_H and low Q_L classification thresholds. The facets are then categorized at each time step T into the three groups: i) H for $Q > Q_H$, ii) L for $Q < Q_L$, and iii) M for $Q_H > Q > Q_L$. The number of occasions when a leaf facet appeared in each of these groups during the simulated day i is counted, resulting in $[N_{H,i}, N_{M,i}, N_{L,i}]$ with $N_{H,i} + N_{M,i} + N_{L,i} = T$. Subsequently, a leaf facet is labelled as sun-adapted (i.e., $C_{f,i} = 1$, with $f \in [1,F]$ where F is the total number of leaf facets) if: i) $N_{H,i} > \frac{T}{2}$ (i.e., leaf facet is categorized as sunlit for the majority of the T time steps), or ii) $N_{M,i} > \frac{T}{2}$ and $N_{H,i} > N_{L,i}$ (i.e., leaf irradiance is, for the majority of T time steps, between the two thresholds and a leaf facet is categorized as sunlit more frequently than shaded). Finally, a leaf facet is labelled as shade-adapted (i.e., $C_{f,i} = 0$) in all other cases, which cover the following three conditions: i) $N_{L,i} > \frac{T}{2}$, ii) $N_{M,i} > \frac{T}{2}$ and $N_{H,i} < N_{L,i}$, and iii) none of the $[N_{H,i}, N_{M,i}, N_{L,i}]$ values dominates during the simulated times. This way, a day series (an array of i values) of sun-adapted ($C_{f,i} = 1$) and shade-adapted ($C_{f,i} = 0$) states is generated per leaf facet f. The final class assignment is decided based on the median value of C_f across the entire examined time period.

The second method uses the probability distribution of the simulated diurnal Q time series. The range of Q values is divided into equally or unequally distributed X intervals, and the Q values of leaf facets simulated at each time step T are categorized in a group x ($x \in [1,X]$). The probability distribution functions of $i \cdot T$ sampling points are then computed over x groups, resulting in the maximum occurrence (i.e., the highest probability density) in group x_{max} and the median occurrence in group x_{median}. A leaf facet is assigned as sun-adapted if $x_{max} > \frac{x}{3}$ and $x_{max} \leq x_{median}$, and shade-adapted in all other cases. Both methods are available in the DART toolbox directory as Python scripts, the decision which to use is solely of user discretion.

To demonstrate changes in SIF_{TOC} due to the distinction of sun- and shade-adapted leaves, we applied two double-threshold classifications on three maize fields (Fig. 1). The first 'relaxed' classification used relatively high and far-apart thresholds of 50 and 100 μmol.photons.m^{-2}.s^{-1}, allowing for a larger portion of shade-adapted parts, whereas the second 'strict' classification used low and close thresholds of 15 and 25 μmol.photons.m^{-2}.s^{-1}, resulting in a smaller amount of strictly shade-adapted leaves and stems. The regularly spaced 1 m tall plants with fully developed bifacial leaves were placed in fields (1 × 1.5 m in size) with a random geographical orientation and distances resulting in LAI = 1, 2 and 4. Specific leaf biochemical, structural and fluorescence properties were assigned to each leaf adaptation class as listed in Table 1 (note that foliage of scenarios without distinct light adaptations was assumed to have the properties of sun-adapted leaves and stems). Contrary to previous SIF simulations, PSII *fqe* values of medium magnitude were assigned to each leaf class, while PSI *fqe* values were kept constant under the assumption that PSI contributes to SIF signal of both leaf types equally (Liu et al., 2019a). In order to prevent its confounding effect, the energy balance (leaf photosynthesis) modelling was disregarded, i.e., the fluorescence efficiency weight *eta* was forced to one. The remaining inputs were arbitrarily defined within plausible dynamic ranges of published laboratory measurements (Hosgood et al., 1994; Jacquemoud and Baret, 1990).

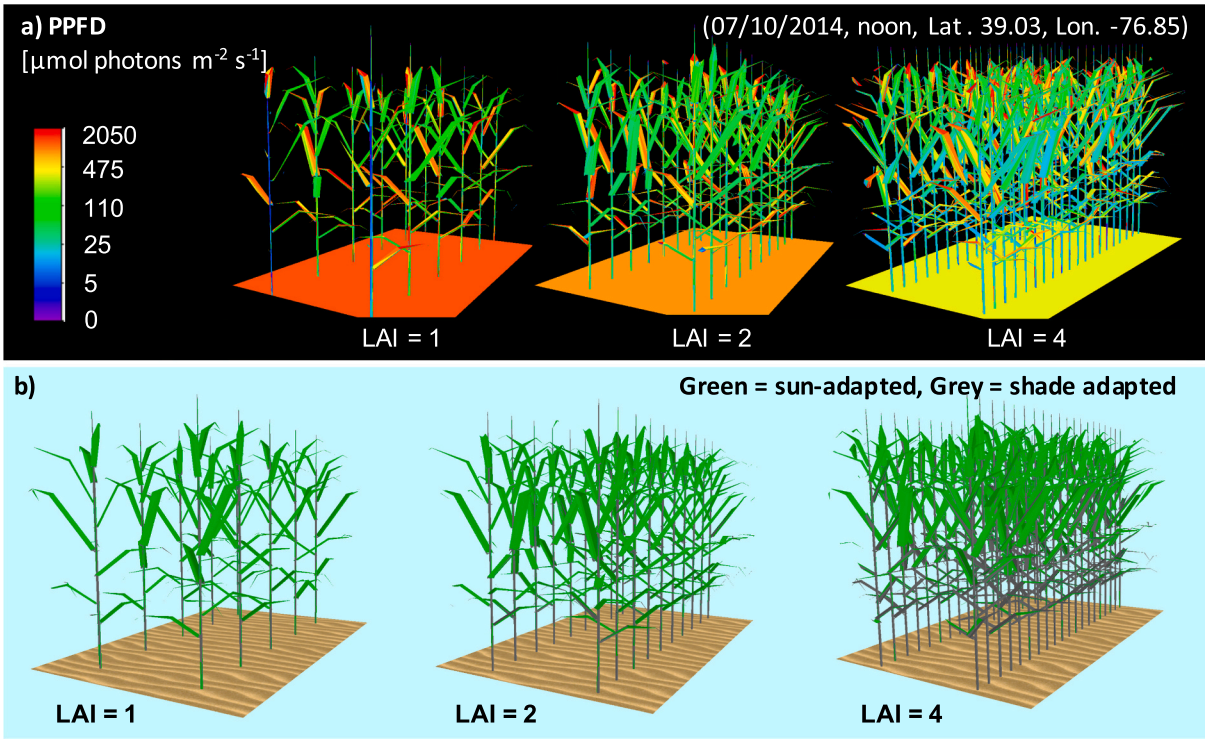

Fig. 1. Incident photosynthetically active radiation expressed in photosynthetic photon flux density (PPFD) for three realistic 3D maize (*Zea mays L.*) canopies with LAI equal to 1, 2 and 4 (a). Distinction of sun- (green) and shade- (grey) adapted foliage based on double PPFD thresholds of 50 and 100 μmol.photons.m^{-2}.s^{-1} (b). To mimic realistic maize canopies, all three maize fields (1 × 1.5 m in size) were created with 1 m tall semi-randomly oriented plants, having eight fully developed bifacial leaves. (For interpretation of the references to colour in this figure legend, the reader is referred to the web version of this article.)

Table 1
Input parameters of the Fluspect-Cx model to simulate optical properties of sun- and shade- adapted leaves, as well as foliage without light adaptations and stems: content of chlorophyll $a + b$ (Cab), total content of carotenoids (Car), equivalent water thickness (EWT), leaf mass per area (LMA), mesophyll optical thickness number (N) and fluorescence quantum efficiencies (*fqe*) for PSI and PSII.

Fluspect inputs	Cab [μg. cm^{-2}]	Car [μg. cm^{-2}]	EWT [cm]	LMA [g. cm^{-2}]	N	PSI *fqe*	PSII *fqe*
Sun-adapted and without adaptation leaves and stems	50	15	0.009	0.0021	1.5	0.002	0.016
Shade-adapted leaves and stems	75	20	0.012	0.0028	2.0	0.002	0.022

2.3.2. Canopy SIF changes due to leaf density and clumping of maize plants

Potential variability in SIF_{TOC} due to leaf density and plant clumping (i.e., canopy closure – CC) changes were simulated for virtual maize canopies of three plant densities (LAI = 1, 2 and 4) in a regular spatial distribution (CC ≈ 100%) and in two clumped formations (LAI = 1 and 2, CC ≈ 50%) (Fig. 2). Compared to the previous exercise (Fig. 1), distances between 6 (LAI = 1) or 12 (LAI = 2) of neighbouring regularly spaced plants in a row were shortened by half to create regular foliage clumps and canopy gaps of the same size. To keep consistency, the leaf and stem optical properties were those used for the turbid-like canopies (Table A1) and the sun- and shade-adaptations were not distinguished, i.e., all leaves were considered as equal.

2.3.3. Influence of leaf clumping, trunks and branches on SIF of white peppermint canopies

DART simulations of eucalyptus forest canopies were used to investigate potential impacts of leaf clumping and woody material, i.e., trunks and branches covered by bark, on SIF_{TOC} modelled at 686 and 740 nm. 3D representations of the eucalyptus trees were constructed based on 3D point clouds acquired with the terrestrial laser scanner (TLS) Trimble TX8 (Trimble Inc., USA). Three native white peppermint eucalypts of different age, height and general habitus were scanned from several geolocations in dry sclerophyll forest located southeast of Hobart (Tasmania, Australia) to acquire their TLS point clouds with a point spacing of 11.3 mm at distance of 30 m. The TLS points of each tree were, after a mandatory pre-processing, semi-automatically separated in two groups: i) points of trunks and branches and ii) points representing foliage. Points classified as wood were used as attractors in an automatic procedure (Sloup, 2013) to extract the external surfaces of trunks and main branches, as described in Verroust and Lazarus (1999). The foliage points were subsequently spatially collocated with the reconstructed wooden skeleton. 3D representation of leaves was created in Blender (Blender, 2007) based on an average shape and size of actual leaves and then distributed automatically at the locations of foliage points according to the Erectophile LAD (Danson, 1998), targeting two crown LAI values of 2 and 5. A complete description of this TLS-based 3D construction of trees, developed specifically for RTM purposes, is available in Janoutová et al. (2019). Two DART canopies (scenes), were constructed with the 3D tree representations: i) a dense canopy was created by placing three trees with the individual crown LAI = 2 within a scene of 81 m^2, while keeping CC ≈ 80% (Fig. 3a), and ii) a sparse canopy was built by redistributing the same trees but with the crown LAI = 5 within a scene of 196 m^2 to achieve CC ≈ 40%. Combinations of the tree crown LAI and scene sizes ensured that both scenes had, for the purpose of comparability, the same canopy LAI = 2.5. Additionally, an identical bark directional-hemispherical reflectance ($\rho \approx 20\%$ at 550 nm, $\rho \approx 40\%$ at 686 nm and $\rho \approx 50\%$ at 740 nm), measured on actual bark samples collected in field, was applied in both canopies.

Besides standard forest canopies (e.g., Fig. 3c), the virtual environment of the DART model also allows for simulating canopies composed of only foliage without woody components (Fig. 3b). By comparing results from simulations with and without woody material, we quantified the magnitudes of shading and direct obstructing effects of woody material. Removing woody components increases the within-canopy iPAR (Q) due to the reduction in wood shadowing, which in turn increases SIF emitted by all previously shaded leaves. The obstruction impact of woody material is caused by its optical interactions with SIF photons. First, it diminishes (blocks) the within-canopy SIF at both 686 and 740 nm via bark scattering and absorption. Second, it affects, to some extent, SIF emission through reflection of SIF at 686 nm that can be reabsorbed and later reemitted by chlorophyll pigments.

2.4. Computation of canopy $fAPAR_{green}$, SIF balance, escape factors and differences

The main driver of green foliage SIF emissions (including stems of the maize plants) in DART simulations that do not contain a modulation of PSI and PSII *fqe* values by *eta* coefficients is the fraction of absorbed photosynthetically active radiation ($fAPAR_{green}$). Therefore, a change of $fAPAR_{green}$ in these simulations indicates a change in the ratio of sunlit and shaded photosynthetically active plant parts, which results in an equal relative change in SIF leaf emission of both photosystems. To be able to investigate the impact of different 3D canopy architectures on their $fAPAR_{green}$, we calculated $fAPAR_{green}$ for all SIF_{TOC} simulating scenarios from the DART radiative budget of a single broad PAR band (λ = [400750] nm) as:

$$\mathrm{fAPAR}(\lambda)_{\mathrm{green}} = \frac{\mathrm{APAR}(\lambda)_{\mathrm{green}}}{\mathrm{PAR}(\lambda)_{\mathrm{TOC}}} \quad (6)$$

where $\mathrm{APAR}(\lambda)_{\mathrm{green}}$ is PAR absorbed by all green plant constituents of a given DART scene and $\mathrm{PAR}(\lambda)_{\mathrm{TOC}}$ is the solar incoming PAR simulated at the top of canopy. The relative difference [%] in $fAPAR_{green}$ of clumped (C) compared to regularly spaced (R) maize canopies was calculated as:

$$\varepsilon_{\mathrm{fAPAR}(\lambda)} = 100.\frac{\mathrm{fAPAR}(\lambda)_{\mathrm{green\_C}} - \mathrm{fAPAR}(\lambda)_{\mathrm{green\_R}}}{\mathrm{fAPAR}(\lambda)_{\mathrm{green\_R}}} \quad (7)$$

Similarly, the shading effect of woody components on eucalyptus SIF emissions was assessed through the relative difference [%] of canopy $fAPAR_{green}$ obtained for simulations containing just foliage (F) and foliage with wood (FW) as follows:

$$\varepsilon_{\mathrm{fAPAR}(\lambda)} = 100.\frac{\mathrm{fAPAR}(\lambda)_{\mathrm{green\_F}} - \mathrm{fAPAR}(\lambda)_{\mathrm{green\_FW}}}{\mathrm{fAPAR}(\lambda)_{\mathrm{green\_FW}}} \quad (8)$$

DART-simulated 3D radiative budget of SIF allows for locating origins of remotely sensed SIF using the SIF balance ($SIF(\lambda)_{bal}$) [$W.m^{-2}.\mu m^{-1}$], computed by subtracting the absorbed SIF flux from the total emitted SIF flux (i.e., $SIF(\lambda)_{PSI}$ plus $SIF(\lambda)_{PSII}$) of a given wavelength (λ) per a vertical canopy layer. A positive $SIF(\lambda)_{bal}$ means that the canopy layer acts as a SIF source, while a negative $SIF(\lambda)_{bal}$ indicates canopy parts acting as SIF sinks. Subsequently, relative difference [%] of SIF $(\lambda)_{bal}$ between clumped (C) and regularly spaced (R) maize canopies, computed as:

$$\varepsilon_{\mathrm{SIF}(\lambda)\mathrm{bal}} = 100.\frac{\mathrm{SIF}(\lambda)_{\mathrm{bal\_C}} - \mathrm{SIF}(\lambda)_{\mathrm{bal\_R}}}{\mathrm{SIF}(\lambda)_{\mathrm{bal\_R}}} \quad (9)$$

reveals if the maize foliage clumping causes a further reduction ($\varepsilon_{SIF(\lambda)bal} < 0$) or an enhancement ($\varepsilon_{SIF(\lambda)bal} > 0$) or no change ($\varepsilon_{SIF(\lambda)bal} = 0$) of SIF balance per a canopy layer.

The proportion of SIF photons that exit the top of canopy is described by the SIF_{TOC} escape probability factor (SIF_{esc}). In practice, this is the ratio of SIF photons escaping from the top of canopy in any direction to

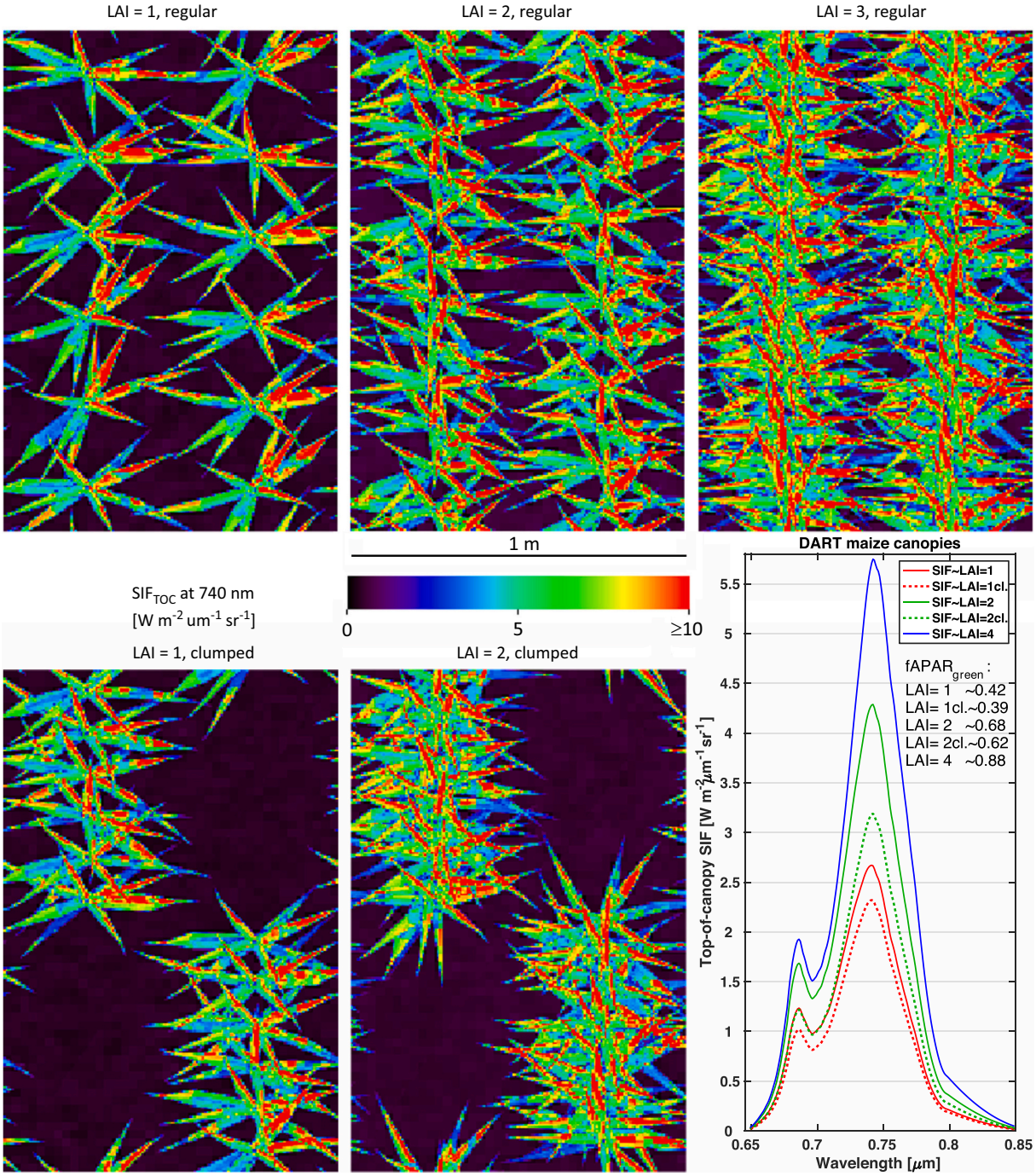

Fig. 2. DART simulated images of top-of-canopy SIF at 740 nm for maize fields of three leaf area indices (LAI) and two canopy closures, 100% regular (top) and 50% clumped (bottom), given by the number of plants (LAI = 1– 12 plants, LAI = 1– 24 plants and LAI = 4– 50 plants) associated with different plant distances. The graph (bottom-right) displays the corresponding modelled canopy SIF spectra between 650 and 850 nm and provides the fAPAR$_{green}$ values per scenario.

all SIF photons emitted from all canopy leaves in forward or backward directions (Guanter et al., 2014). SIF$_{esc}$ is required for scaling of SIF$_{TOC}$ measurements down at the spatial level of individual leaves (van der Tol et al., 2019), and subsequently essential for correct estimation of vegetation gross primary production (GPP) from airborne and space-borne SIF observations (e.g., He et al., 2017; Zhang et al., 2020). Since most of RS observations capture SIF$_{TOC}$ from nadir, we computed the relative canopy SIF escape probability factor of a given wavelength (λ) in the nadir direction (SIF*nadir*(λ)$_{esc}$) from SIF radiative budgets of the eucalyptus scenarios. First, we converted SIF emissions of PSI and PSII per m^2 of abaxial and adaxial leaf facets into SIF emissions per m^2 of the scene (F(λ)$_{PSI}$ and F(λ)$_{PSII}$) [W.m^{-2}.μm^{-1}] and then calculated SIF*nadir* (λ)$_{esc}$ as:

$$\mathrm{SIF}nadir(\lambda)_{esc} = \frac{\pi \cdot \left(\mathrm{L}nadir(\lambda)_{PSI} + \mathrm{L}nadir(\lambda)_{PSII}\right)}{\mathrm{F}(\lambda)_{PSI} + \mathrm{F}(\lambda)_{PSII}} \quad (10)$$

where L*nadir*(λ)$_{PSI}$ and L*nadir*(λ)$_{PSII}$ [W.m^{-2}.μm^{-1}.sr^{-1}] are DART modelled PSI and PSII SIF radiances at the wavelength (λ), respectively, escaping from the simulated scene in the nadir viewing direction. The π multiplication in Eq. 10 is removing the angular dependency [sr^{-1}], resulting in relative values of SIF*nadir*(λ)$_{esc}$ between 0 and 1. Since the

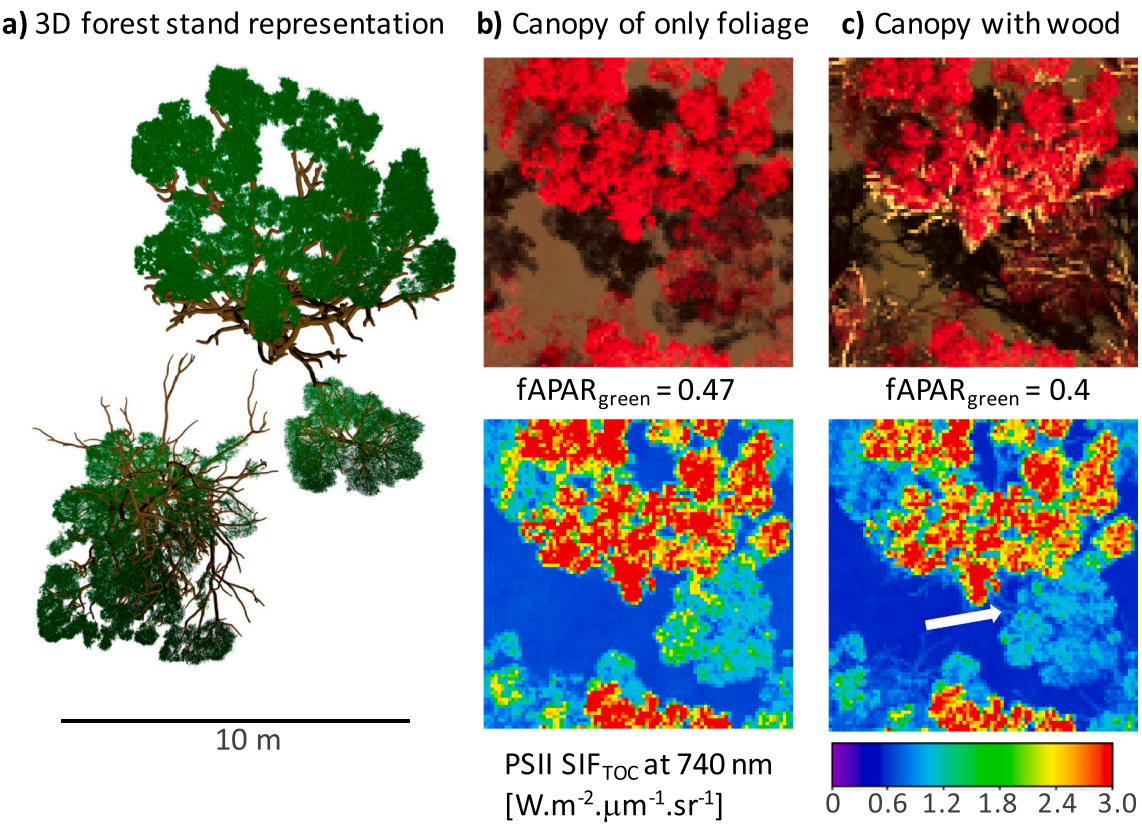

Fig. 3. Nadir view of 3D representation of the dense white peppermint (*Eucalyptus pulchella*) test canopy derived from terrestrial laser scans of trees growing east of Hobart (Tasmania, Australia) (a). The virtual scene (LAI = 2) was used to simulate a near-infrared, red and green RGB false colour composite images in DART of top-of-canopy reflectance (top) as well as PSII SIF at 740 nm (bottom) of the canopy formed by: b) only foliage and c) foliage and woody material covered with bark. The white arrow points at the example of SIF reflection from an exposed tree branch surface. (For interpretation of the references to colour in this figure legend, the reader is referred to the web version of this article.)

escape probability factor is predominantly dependent on direct optical interactions with canopy elements that attenuate an emitted SIF signal, we quantified the obstruction (blocking) effect of eucalyptus woody components on canopy SIF in the nadir viewing direction through the relative difference [%] of SIF*nadir*$(\lambda)_{esc}$, computed from the foliage only (F) and the foliage with wood (FW) simulations as follows:

$$\varepsilon_{SIF(\lambda)esc} = 100.\frac{SIFnadir(\lambda)_{esc\_F} - SIFnadir(\lambda)_{esc\_FW}}{SIFnadir(\lambda)_{esc\_FW}} \quad (11)$$

Finally, to analyse differences in SIF fluxes escaping from individual simulated canopy layers in all directions (i.e., towards layers of the upper and lower hemispheres), we computed from DART 3D radiative budget their relative omnidirectional escape factor (SIF*omni*$(\lambda)_{esc}$) as:

$$SIFomni(\lambda)_{esc} = \frac{\left(F(\lambda)_{PSI} + F(\lambda)_{PSII}\right) - \left(A(\lambda)_{PSI} + A(\lambda)_{PSII}\right)}{F(\lambda)_{PSI} + F(\lambda)_{PSII}} \quad (12)$$

where A$(\lambda)_{PSI}$ and A$(\lambda)_{PSII}$ [W.m^{-2}.µm^{-1}] are DART modelled absorptances of PSI and PSII SIF, respectively, expressed for the wavelength (λ) per m^2 of the scene. If SIF*omni*$(\lambda)_{esc} \leq 0$, then the canopy layer does not contribute to the SIF$_{TOC}$ signal, i.e., its SIF$(\lambda)_{bal}$ is either neutral or negative.

2.5. DART settings common to all SIF canopy simulations

DART simulations were carried out with the flux-tracking algorithm using the following settings: no elimination of low energy rays, relative accuracy on scene albedo equal to 10^{-6}, 25 duplications of the initially simulated scene, the scene illumination mesh size equal to 5.10^{-4} m (with a semi-random spatial distribution of illumination rays), and cell sub-sampling with 8^3 sub-cells per cell and 1 sub face per cell face. An optimal number of 20 flux-tracking iterations, which were required to obtain a 10^{-2} relative accuracy of the scene reflectance, was determined through a simplified accuracy sensitivity study. Intermediate results of the last few iterations were used to extrapolate the final values of simulated radiative budget, bidirectional reflectance function and SIF products. TOC reflectance and SIF were simulated in 212 viewing directions (Yin et al., 2013), distributed systematically throughout the upward hemisphere, with an oversampling of the upward hot-spot region (25 directions in a solid angle of 0.01 sr around the hotspot direction) and 34 virtual viewing directions in the solar principle plane. Leaf facets were simulated as double-faces without the solar penumbra effect, all optical properties were assumed to be Lambertian, and the scene ground surface was horizontal.

2.6. Comparative statistical indicators

Comparative statistical indicators, specifically a root mean square error (RMSE) and an index of agreement (d), were computed to assess these similarities as well as anticipated statistical dissimilarities between different DART scenarios (i.e., turbid-like vs. maize and eucalypt canopies). As explained in Willmott (1981), the dimensionless index of agreement complements the RMSE by indicating the degree of correspondence between two tested datasets in magnitude and direction, where d = 1 means full agreement and d = 0 means total disagreement. Also, the similarity of DART and SCOPE multi-angular SIF$_{TOC}$ was assessed through fitting a linear regression model, where the regression coefficient of determination (R^2) indicated how much of the variability in a reference RT model (i.e., SCOPE) results can be explained by corresponding regressed values simulated in DART.

3. Results

3.1. Comparison of nadir DART and SCOPE/mSCOPE canopy SIF simulations

The SCOPE and DART nadir SIF_{TOC} signatures of turbid medium vegetation canopies were nearly identical (Fig. A2). Results between 641 and 850 nm were comparable for all simulated input combinations (i.e., three LAI, three LAD and three soil types). High SIF_{TOC}, observed for canopies of Planophile LAD, is caused by their high PAR interception efficiency. The highest RMSE = 0.162 $W.m^{-2}.\mu m^{-1}.sr^{-1}$ and the lowest d = 0.9965 were found for the Erectophile canopy of LAI = 1, covering soil with $\rho = 50\%$. Despite being the worst case, the values indicate only minor differences between DART and SCOPE results. Statistical analyses revealed that the total SIF_{TOC} RMSE originates mainly from RMSE for PSII, which was twice the RMSE for PSI simulations for all three LADs (results not shown). Despite a significantly higher variability in RMSE than other two LADs, the Planophile LAD showed the highest index of agreement and R^2 computed between the two models.

mSCOPE allowed us to introduce a biochemical/optical heterogeneity in the vertical dimension of simulated canopies. Additionally, we tested DART SIF simulation performance when using the energy balance *eta* coefficients produced by mSCOPE. Comparison of total nadir SIF_{TOC} radiances produced by both models revealed almost the same results (Fig. A3). The indices of agreement were in all cases larger than 0.99, regardless exclusion or inclusion of the mSCOPE *eta* coefficients in conducted simulations. The highest RMSE of just 0.221 $W.m^{-2}.\mu m^{-1}.sr^{-1}$ and the lowest d = 0.9985 was found for simulation of 2-layered canopy with LAI = 2 and with the leaf energy balance included (Fig. A3b).

3.2. Multi-angular comparison of DART and SCOPE canopy SIF simulations

The similarity of DART and SCOPE SIF_{TOC} simulations at 686 and 740 nm was also investigated for viewing directions other than the nadir view. We compared values simulated in the solar principal plane, with particular attention to the hotspot region, and computed absolute differences between 27 DART and SCOPE turbid medium scenarios in all 212 viewing directions. The smallest differences and the best agreement were found for SIF_{TOC} at 686 nm, Erectophile LAD and LAI = 1 (Fig. A4), while the worse agreement and largest differences were obtained for SIF_{TOC} at 740 nm, Spherical LAD and LAI = 4 (Fig. A5). Here, SCOPE simulated slightly smaller SIF_{TOC} values, except for VZA > 75°, where SIF_{TOC} dropped unexpectedly steeply down. Also, SCOPE values around the hotspot angles were about 1 $W.m^{-2}.\mu m^{-1}.sr^{-1}$ lower than the corresponding DART values. This is caused by differences in the vegetation hotspot algorithms. SCOPE uses a Kuusk's analytical approximation, which does not account for a bi-directional gap-fraction correlation with the canopy depth and consequently underestimates the hotspot effect (Kallel and Nilson, 2013), whereas hotspot in DART simulations is physically modelled.

Analysis of multi-angular SIF differences among the three LADs stressed smaller dissimilarities at 686 nm, having the best fit for the Spherical LAD, followed by the Erectophile LAD, and then by the Planophile LAD. At 740 nm, the closest match occurred for the Planophile LAD, while the Spherical and the Erectophile LADs showed equal discrepancies (Fig. A6). Nonetheless, the maximal absolute SIF_{TOC} difference between DART and SCOPE oblique viewing directions of all scenarios was found to be <0.8 $W.m^{-2}.\mu m^{-1}.sr^{-1}$.

3.3. Effect of sun- and shade-adapted maize foliage classification

Two double-threshold classifications were used to assess the impact of sun- and shade-adapted foliage differentiation on nadir PSI and PSII SIF_{TOC} between 650 and 850 nm. The first one, called 'relaxed', used the far-apart high Q thresholds (50 and 100 μmol.photons.$m^{-2}.s^{-1}$), resulting in the sun-to-shade adapted foliage ratio ranging from 80:20% (LAI = 1) to 55:45% (LAI = 4). Fig. 4a shows that differences between SIF_{TOC} signatures for simulations with and without the differentiation of sun−/shade-adapted leaves were all positive for PSII, with the highest value ≈ 0.1 $W.m^{-2}.\mu m^{-1}.sr^{-1}$ around 740 nm for LAI = 4 ($fAPAR_{green}$ = 0.87). Surprisingly, the same differences for PSI between 700 and 725 nm were negative, demonstrating a greater PSI SIF absorption by shade-adapted leaves having a higher chlorophyll $a + b$ content of 75 $\mu g.cm^{-2}$. Contrary to PSII SIF_{TOC}, where *fqe* was increased from 0.016 to 0.022 for shade-adapted leaves (Table 2), the constant PSI *fqe* of 0.002 could not compensate this increased chlorophyll absorption. The second classification, called 'strict', used the closer and lower Q thresholds (15 and 25 μmol.photons.$m^{-2}.s^{-1}$), resulting in canopies with a dominant portion of sun-adapted leaves. The sun-to-shade adapted foliage ratio ranged from 98:2% (LAI = 1) to 73:27% (LAI = 4). Consequently, the SIF_{TOC} differences were proportionally smaller (Fig. 4b), with the largest value of 0.035 $W.m^{-2}.\mu m^{-1}.sr^{-1}$ for PSII SIF_{TOC} at 740 nm (LAI = 4). PSI SIF_{TOC} differences were also reduced and remained negative between 700 and 725 nm.

3.4. Influence of foliage density and clumping in maize canopies

Fig. 2 illustrates the impact of a leaf density increase (i.e., doubled LAI) and the clumping of maize plants for LAI of 1 and 2. Nadir images of maize canopy SIF_{TOC} at 740 nm show the spatial dependence of SIF_{TOC} radiance on the absorption of iPAR and on the distribution of plant shadows. A linear increase of LAI triggered a non-linear and wavelength-specific increase of SIF_{TOC}. A bit more than 2-fold increase in far-red wavelengths from LAI = 1 to LAI = 4 corresponds to a similar increase in canopy $fAPAR_{green}$, which is not the case for the red SIF_{TOC} nadir signal (Fig. 2). The canopy clumping causes a decrease of SIF_{TOC} at all wavelengths. The 50% decrease in CC caused SIF_{TOC} reduction at 740 nm of about 0.4 for LAI = 1 and 1.0 $W.m^{-2}.\mu m^{-1}.sr^{-1}$ for LAI = 2, whereas reduction of LAI from 2 to 1 resulted in larger SIF_{TOC} declines of about 0.75 for CC = 50% and 1.6 $W.m^{-2}.\mu m^{-1}.sr^{-1}$ for CC = 100%.

The interpretation of canopy architectural effects can be taken further by investigating the multi-angular differences for SIF_{TOC} at 686 (Fig. 5) and 740 nm (Fig. 6), computed between the turbid-like vegetation canopy, i.e., a random distribution of many small leaf facets with the Spherical LAD, and the maize regular and clumped canopies of much larger leaves, both with LAI = 2. DART simulated multi-angular SIF_{TOC} values of the turbid-like and regular maize canopies at 686 nm are very close (RMSE = 0.27 $W.m^{-2}.\mu m^{-1}.sr^{-1}$, d = 0.9) (see Fig. 5ac), indicating rather similar SIF absorptions within canopies and by soil. The maximum difference of just about −0.4 $W.m^{-2}.\mu m^{-1}.sr^{-1}$ appeared in very oblique viewing directions, in which maize plants scattered less SIF. Despite its slightly lower $fAPAR_{green}$ (0.68 vs. 0.72), the maize canopy scattered a bit more SIF in viewing directions around nadir and hotspot, producing a positive difference. This is caused by the maize geometrically explicit non-random LAD and large-sized leaf facets, redirecting the scattered SIF prevailingly in these directions. Larger size of maize leaves is decreasing scattering of photons, and consequently the diffuse fluxes, and causing a broader base of the SIF_{TOC} hotspot peak, observed when comparing the hotspots regions of maize and the turbid-like medium simulations. Although the multi-angular pattern for the clumped maize canopy looks also very similar (RMSE = 0.36 $W.m^{-2}.\mu m^{-1}.sr^{-1}$, d = 0.81), the differences are all negative and significantly larger, with the maximum of about −0.75 $W.m^{-2}.\mu m^{-1}.sr^{-1}$ (Fig. 5bd). It means that the 50% foliage clumping increased scattering and the subsequent within-canopy absorption of SIF at 686 nm, because SIF absorption by the loamy soil beneath the clumped canopy was 7% lower than in the regular canopy, i.e., unable to cause the SIF_{TOC} reduction. The angular distributions of the same differences at 740 nm look different (Fig. 6), as they are ruled mainly by scattering related to the canopy architecture. The decrease in intensity of maize far-red SIF_{TOC} is driven by the species-

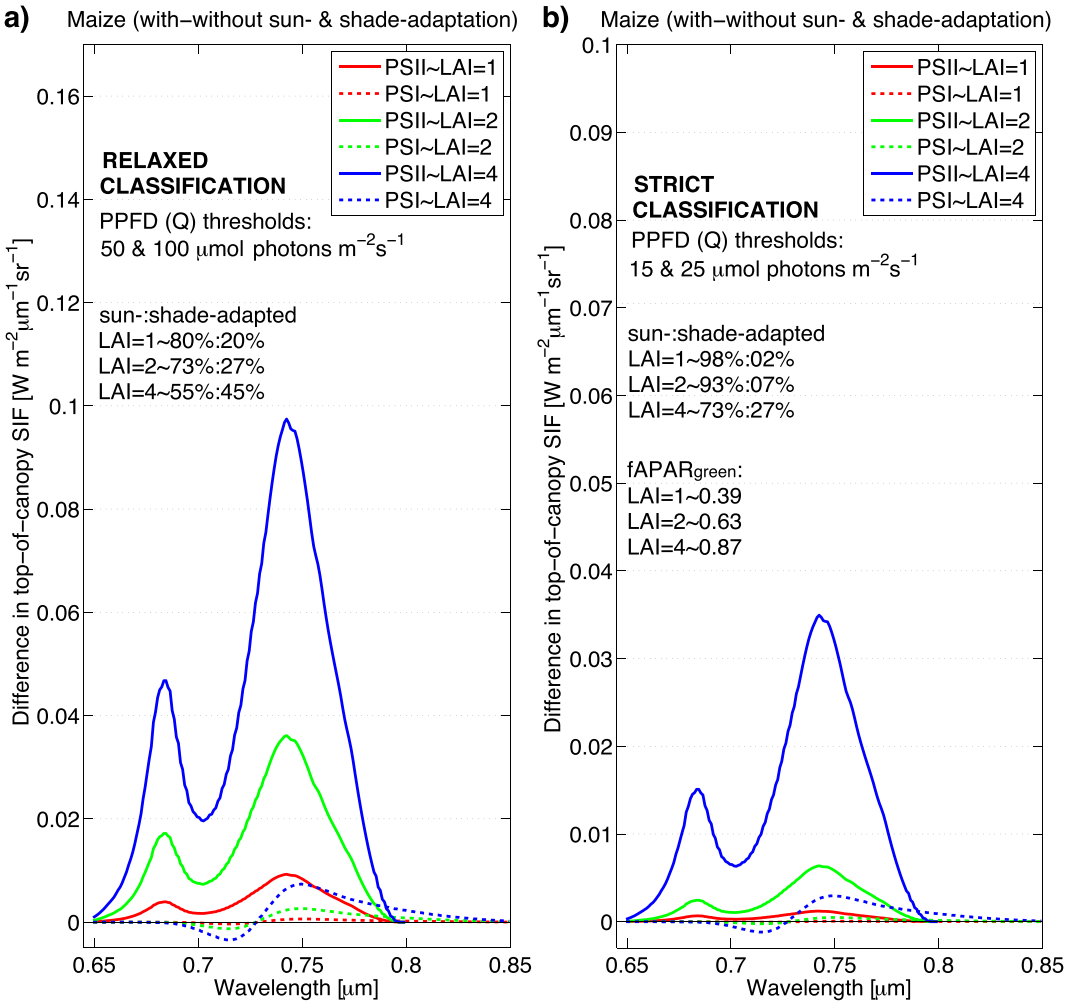

Fig. 4. Differences in DART top-of-canopy SIF radiance due to distinction of sun- and shade-adapted leaves of regular maize canopies with LAI = 1, 2 and 4. Graphs illustrate two simulated scenarios of photosynthetic photon flux density (PPFD or Q) classification thresholds: a) a 'relaxed' scenario with high PPFD thresholds of 50 and 100 μmol.photons.m^{-2}.s^{-1}, and b) a 'strict' scenario with low PPFD thresholds of 10 and 25 μmol.photons.m^{-2}.s^{-1}. For details about the double-threshold leaf light adaptation classification see Section 2.3.1.

Table 2
DART simulated impacts of woody material and bark on $fAPAR_{green}$ of leaves, SIF leaf emissions, nadir top-of-canopy SIF_{TOC} and nadir SIF escape probability factor at 686 and 740 nm of two white peppermint (*Eucalyptus pulchella*) stands with dense and sparse canopy covers (CC) and LAI = 2.5. The relative impact on canopy SIF emitted by leaves (Bold fonts), is caused either by shadows casted on photosynthetically active foliage (*shading effect*; Eq. 8) or by absorption and scattering of SIF photons by bark-covered wood in combination with green foliage (*obstruction effect*; Eq. 11); (↓) indicates a decreasing and (↑) an increasing effect.

DART scenario	Dense canopy (CC ≈ 80%)			Sparse canopy (CC ≈ 40%)		
DART outcome	Foliage only	Foliage & Wood	Relative impact [%]	Foliage only	Foliage & Wood	Relative impact [%]
$fAPAR_{green}$ of leaves	0.466	0.399		0.306	0.279	
Shading effect $\varepsilon_{fAPAR(400-750)}$			**17.0 (↓)**			**9.7 (↓)**
Red SIF (686 nm)						
Emitted by leaves [W.m^{-2}.μm^{-1}]	11.626	9.939		7.618	6.945	
Nadir SIF_{TOC} [W.m^{-2}.μm^{-1}.sr^{-1}]	0.554	0.481		0.303	0.275	
$SIF_{nadir}(686)_{esc}$ [rel.]	0.150	0.152		0.125	0.124	
Obstruction effect $\varepsilon_{SIF(686)esc}$			**-1.5 (↑)**			**0.6 (↓)**
Far-red SIF (740 nm)						
Emitted by leaves [W.m^{-2}.μm^{-1}]	24.461	20.914		16.029	14.613	
Nadir SIF_{TOC} [W.m^{-2}.μm^{-1}.sr^{-1}]	2.093	1.693		1.260	1.108	
$SIF_{nadir}(740)_{esc}$ [rel.]	0.269	0.254		0.247	0.238	
Obstruction effect $\varepsilon_{SIF(740)esc}$			**5.7 (↓)**			**3.6 (↓)**

specific foliage distribution and geometry, significantly larger maize leaf size combined with a high leaf single scattering albedo at 740 nm and the soil absorption. SIF_{TOC} differences in Fig. 6 are negative for both regular (RMSE = 0.42 W.m^{-2}.μm^{-1}.sr^{-1}, d = 0.92) and clumped canopy of LAI = 2, but larger for the latter one (RMSE = 1.22 W.m^{-2}.μm^{-1}.sr^{-1}, d = 0.62). Results of DART radiative budget revealed that the introduction of clumping did not increase but lowered (by 12%) the amount of soil intercepted and absorbed SIF. Hence, it is not soil but clumping-

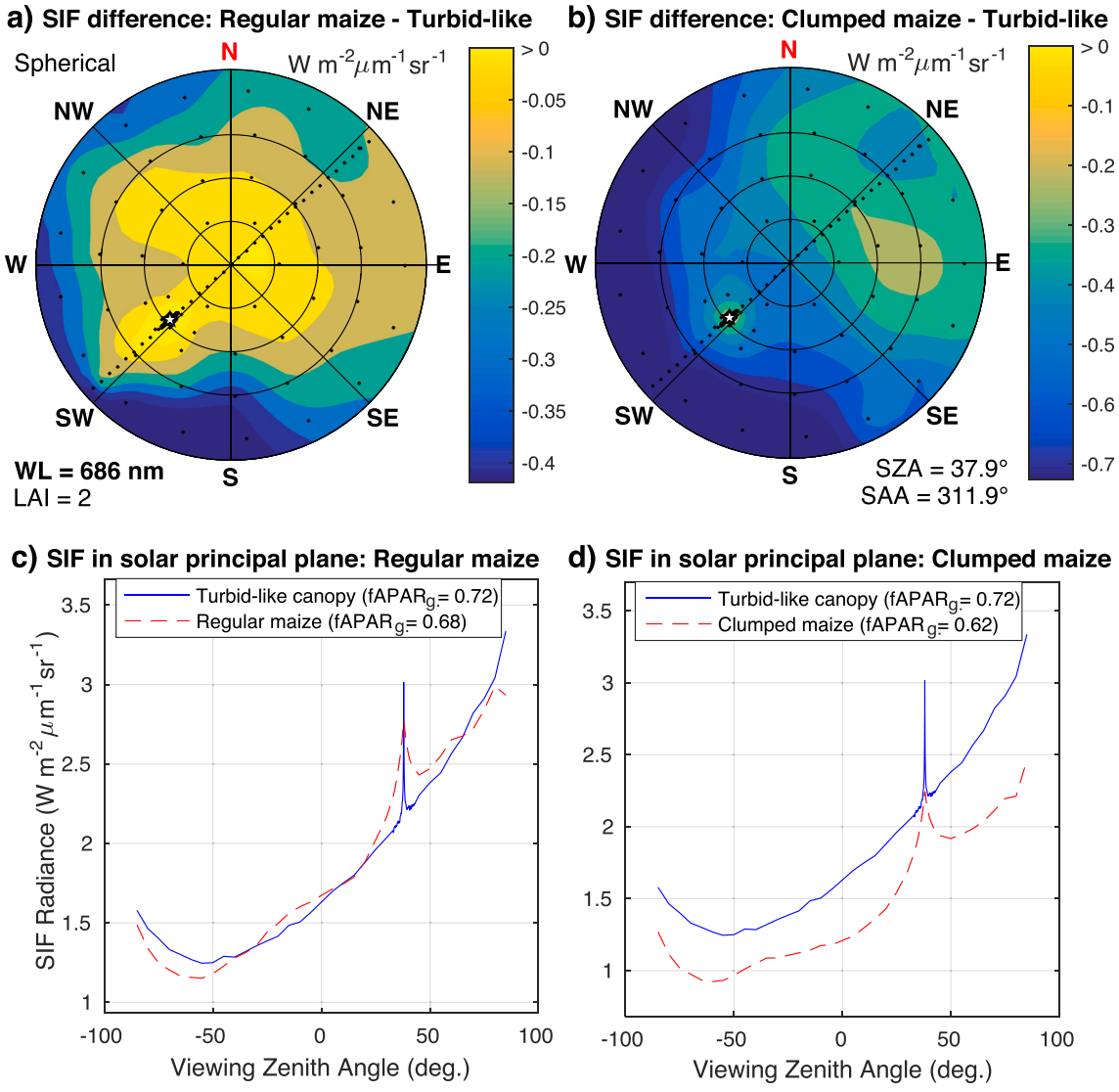

Fig. 5. Multi-angular differences in SIF radiance at 686 nm between a) regular, b) clumped DART 3D maize canopies and a DART simulated turbid-like canopy with LAI = 2, Spherical LAD and loamy soil as ground. SIF radiances in the solar principal plane for the turbid-like canopy together with the regular (RMSE = 0.27 and d = 0.9) and the clumped (RMSE = 0.36 and d = 0.81) maize canopies are illustrated in c) and d), respectively. Notations: the white star shows the solar position and black dots indicate the simulated viewing directions; LAD ~ leaf angle distribution; LAI ~ leaf area index; WL ~ wavelength; SZA ~ solar zenith angle; SAA ~ solar azimuth angle; R^2 ~ coefficient of determination; RMSE ~ root mean square error [$W.m^{-2}.\mu m^{-1}.sr^{-1}$]; d ~ index of agreement: 0 = no agreement, 1 = full agreement.

induced within canopy SIF optical interactions that are responsible for this extra reduction of SIF_{TOC}.

The relative contribution from different canopy parts (horizontal layers) to SIF_{TOC} and its modulation by $fAPAR_{green}$ or by SIF scattering and absorption can be investigated by plotting vertical canopy height profiles of $fAPAR_{green}$ together with corresponding SIF balances of both fluorescence wavelengths. Fig. 7a shows that SIF balances are positive at all heights, i.e., every layer act as a SIF source, and they follow, in general, changes in $fAPAR_{green}$. The foliage clumping decreased significantly $fAPAR_{green}$, $SIF(\lambda)_{bal}$ and also $SIFomni(\lambda)_{esc}$ (not shown) in the upper half of the canopy with LAI = 2, causing the overall reduction of SIF_{TOC}, but it increased all of them in canopy parts below. It means that the lower leaves of the clumped canopy contributed to the simulated SIF_{TOC} more than the same leaves of the regular canopy.

Fig. 7b, depicting the $fAPAR_{green}$ and $SIF(\lambda)_{bal}$ relative differences between the regular and clumped canopies, provides a further insight in this behaviour and dependencies between SIF and $fAPAR_{green}$ radiative budgets. It illustrates a clumping-induced steady reduction of $fAPAR_{green}$ and SIF balance differences in upper 40% of the canopy with LAI = 1, whereas the differences in lower 60% fluctuate between positive and negative values. $\varepsilon_{SIF(740)bal}$ for LAI = 1 follows quite closely $\varepsilon_{fAPAR(\lambda)}$, suggesting that variability of SIF fluxes at 740 nm is ruled mainly by clumping-induced changes in distribution of shadows and sun flecks, while $\varepsilon_{SIF(686)bal}$ shows a bit more negative or positive deviations from $\varepsilon_{fAPAR(\lambda)}$, caused by a local increase or decrease in chlorophyll absorption of SIF at 686 nm. SIF_{TOC} for LAI = 2 is formed by steady but greater negative differences in the canopy top half that are partially balanced out by nearly 2-fold larger positive differences between 30 and 50% of the canopy relative height. Comparable differences for both LAI cases between the bottom and 30% of the canopy height indicate very similar $fAPAR_{green}$ and SIF radiative budgets, driven by mostly diffused low-intensity PAR. The negative $\varepsilon_{fAPAR(\lambda)}$ and $\varepsilon_{SIF(\lambda)bal}$ values in the upper half of the canopy are caused by combination of higher (doubled) LAI with foliage clumping that increased internal shadowing and consequently reduced $fAPAR_{green}$. It also enhanced a number of SIF photons interacting with leaf facets, resulting in a higher fluorescence

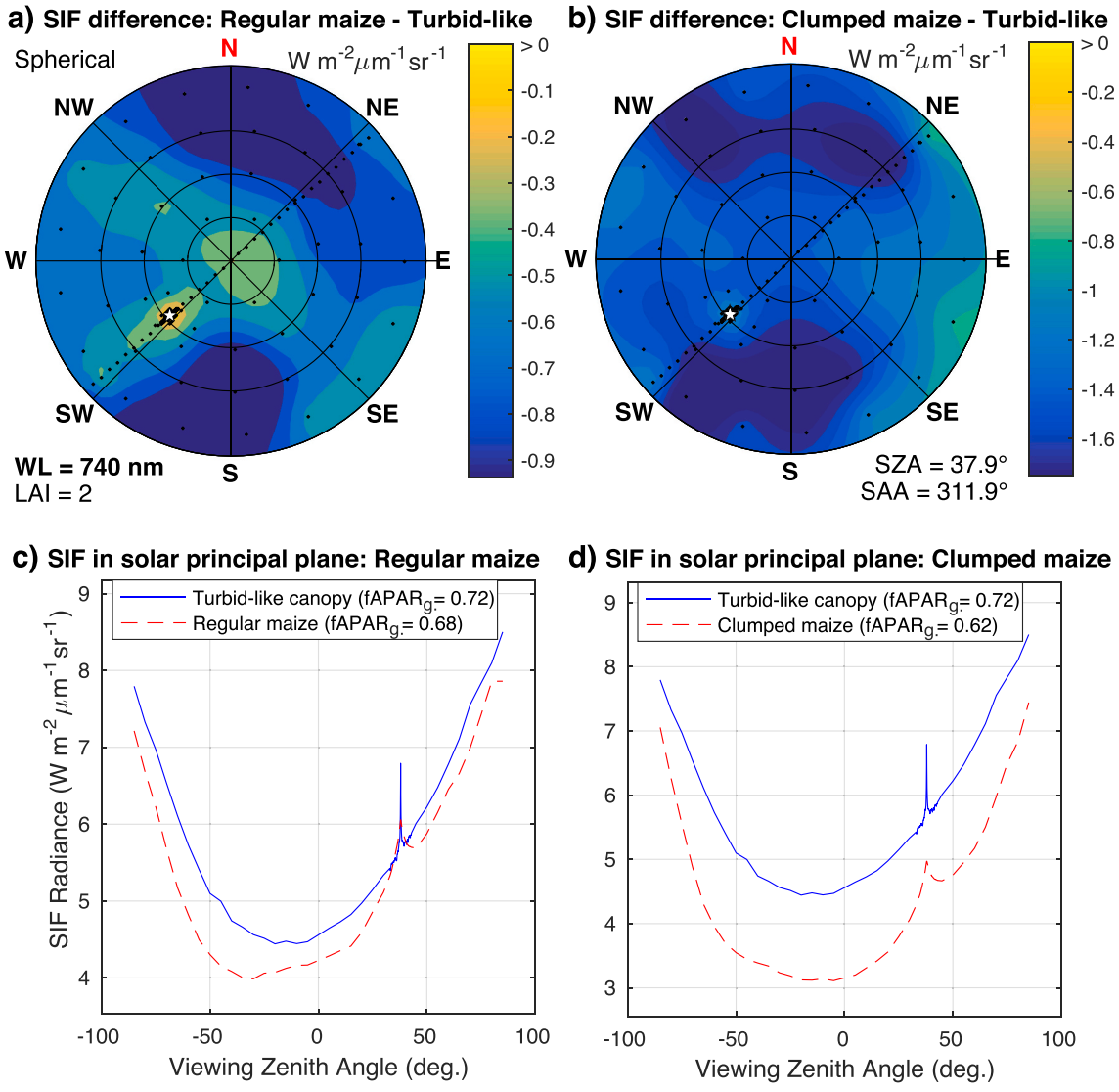

Fig. 6. Multi-angular differences in SIF radiance at 740 nm between a) regular, b) clumped DART 3D maize canopies and a DART simulated turbid-like canopy with LAI = 2, Spherical LAD and loamy soil as ground. SIF radiances in the solar principal plane for the turbid-like canopy together with the regular (RMSE = 0.42 and d = 0.92) and the clumped (RMSE = 1.22 and d = 0.62) maize canopies are illustrated in c) and d), respectively (for abbreviations and symbols see Fig. 5).

absorption, especially at 686 nm. Scientifically interesting is the opposite behaviour between 30 and 50% of the canopy height, where it boosted $fAPAR_{green}$ and consequently SIF emissions, but simultaneously diminished SIF absorption, which is evidenced by $\varepsilon_{SIF(686)bal}$ and $\varepsilon_{SIF(740)bal} > \varepsilon_{fAPAR(\lambda)}$. The total energy released from these positive $SIF(\lambda)_{bal}$ differences was, nevertheless, unable to fully compensate the negative $SIF(\lambda)_{bal}$ differences induced by clumping in the upper canopy parts (Fig. 7a).

3.5. Impacts of foliage clumping and wood of white peppermint trees

DART 3D modelling allowed us to investigate previously unquantified impacts of foliage structure and woody material on $fAPAR_{green}$ and on optical interactions of SIF photons inside white peppermint canopies. Fig. 3 shows nadir PSII SIF_{TOC} images at 740 nm for dense eucalyptus forest canopies without and with presence of the woody parts. A simple visual comparison of the two images reveals a lower SIF_{TOC} in the lower right corner of the image caused by a deeper shadowing after inclusion of trunks and branches. One can also detect several large non-fluorescing branches in the SIF_{TOC} image, visible due to a strong reflection of far-red SIF photons by peppermint bark ($\rho_{740\ nm} \approx 50\%$).

In comparison with the multi-directional SIF radiance of the turbid-like canopy, the dense eucalyptus stand without wood showed statistically significant decreases in SIF_{TOC} at 686 nm (RMSE = 0.82 $W.m^{-2}.\mu m^{-1}.sr^{-1}$, d = 0.55) (Fig. 8ac) and even greater at 740 nm (RMSE = 1.93 $W.m^{-2}.\mu m^{-1}.sr^{-1}$, d = 0.47) (Fig. 9ac). This drop, reaching up to −1.2 $W.m^{-2}.\mu m^{-1}.sr^{-1}$ and almost −2.5 $W.m^{-2}.\mu m^{-1}.sr^{-1}$, respectively, can be explained by the Erectophile LAD of the small-sized narrow white peppermint leaves, and by their strong and spatially irregular clumping at the branch level. Presence of woody structures did not change considerably the angular patterns of the SIF_{TOC} differences, but caused its further suppression at 686 nm (RMSE = 1.0 $W.m^{-2}.\mu m^{-1}.sr^{-1}$, d = 0.47) (Figure 8bd) and even larger differences at 740 nm (RMSE = 2.68 $W.m^{-2}.\mu m^{-1}.sr^{-1}$, d = 0.35) (Figure 9bd). Interestingly, it deepened the shape the solar principal plane SIF_{TOC} curve in back-scattering oblique viewing directions behind the hotspot region, producing the maximum difference of almost −1.4 $W.m^{-2}.\mu m^{-1}.sr^{-1}$ at 686 nm and around −3.7 $W.m^{-2}.\mu m^{-1}.sr^{-1}$ at 740 nm.

The DART ability to simulate forest stands with and without woody elements opened an opportunity for quantification of their potential impacts on SIF emitted, observed and escaped in the nadir direction from white peppermint dense and sparse canopies (Table 2). We

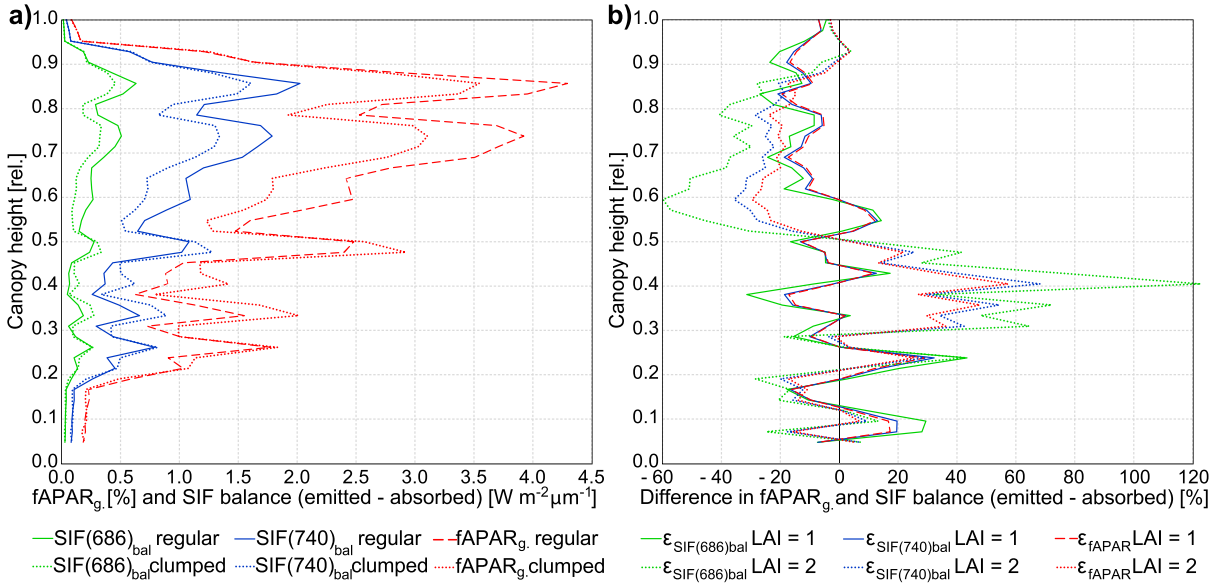

Fig. 7. Vertical profiles of a) fAPAR$_{green}$, SIF balances (for maize canopies of LAI = 2) and b) their relative differences at 686 and 740 nm computed between regularly spaced and clumped canopies of the same LAI (for LAI = 1 and 2). Each 2.5 cm thick canopy layer is presented as a point of the relative canopy height [0–1]. For details about computations of fAPAR$_{green}$, SIF balance (SIF(λ)$_{bal}$) and their relative differences ($\varepsilon_{fAPAR(\lambda)}$ and $\varepsilon_{SIF(\lambda)bal}$) see Section 2.4.

quantified the wood shading effect, causing changes in canopy fAPAR$_{green}$ due to the scattering and absorption of iPAR, and the obstruction (blocking) effect of eucalyptus wood, caused by scattering and absorption of SIF photons by bark. As expected, wood shadowing lowered SIF emitted at both investigated wavelengths by the percentage equal to the fAPAR$_{green}$ reduction, i.e., by 17.0% for the dense and 9.7% for the sparse canopy. Comparison of the foliage only SIF$_{TOC}$ with the foliage and wood SIF$_{TOC}$ revealed lesser impacts at 686 nm than at 740 nm. SIF escape probability factors of the simulated eucalyptus canopies were generally low: SIF*nadir*(686)$_{esc}$ $\leq$ 0.15 and SIF*nadir*(740)$_{esc}$ $\leq$ 0.27. Overall, the wood obstruction effect was greater on far-red than red SIF escape factors, causing a consistent decrease of 4–6% in SIF*nadir*(740)$_{esc}$, but almost no change in SIF*nadir*(686)$_{esc}$ for the sparse and less than 2% increase for the dense canopy (Table 2).

More detailed understanding of the wood-induced effects inside the dense white peppermint canopy can be obtained from analysing its DART-simulated vertical profiles of SIF balances and omnidirectional SIF escape factors. Plots of SIF(λ)$_{bal}$ in Fig. 10a and SIF*omni*(λ)$_{esc}$ in Fig. 10b, shown across the relative stand height, revealed two significant findings. First, every leaf-containing part of the canopy comprised of only foliage is acting as a SIF source (SIF*omni*(λ)$_{esc}$ > 0), but the presence of woody components turned the parts emitting only a little fluorescence into SIF sinks (SIF*omni*(λ)$_{esc}$ = 0). Second, a majority of the SIF$_{TOC}$ signal originates from leaves occupying top 25% percent of the eucalyptus canopy height. Although the close-up of the 0–30% canopy height section in Fig. 10a shows a strong SIF absorption by trunks and lower branches that results in SIF(λ)$_{bal}$ < 0 (especially at 740 nm), different SIF energy budget results were obtained for top 25% (i.e., 75–100%) of the canopy. The wood presence in this highly emitting canopy part increased the SIF(686)$_{bal}$ values only negligibly, as the bark and photosynthesizing leaves were capable of absorbing nearly all extra SIF photons reflected at 686 nm by woody structures. This result is in line with a very slight increase of SIF*nadir*(686)$_{esc}$ listed in Table 2. Wood presence, however, decreased absorptance and increased more than 2-fold reflectance of SIF at 740 nm, which significantly enhanced (almost doubled) the SIF(740)$_{bal}$ values in this upper canopy part. Despite this limited local boost, wood obstructions suppressed values of both SIF(740)$_{bal}$ and SIF*omni*(740)$_{esc}$ in the rest of the canopy profile, leading to an overall 5.7% reduction in canopy SIF*nadir*(740)$_{esc}$ (Table 2) and, consequently, in a decrease of multi-angular SIF$_{TOC}$ (Figure 9ab).

4. Discussion

4.1. Comparison of DART and SCOPE/mSCOPE models

DART outputs were nearly in a perfect agreement with the corresponding results obtained for simple, turbid medium vegetation scenes with SCOPE and mSCOPE. Better agreements were obtained for the SIF$_{TOC}$ local maximum at 686 nm, where the signal is attenuated by the SIF chlorophyll absorption. Since the SIF$_{TOC}$ values at 740 nm are controlled dominantly by canopy structural traits, the smallest discrepancies were obtained for the geometrically more uniform Planophile LAD. Here, the SIF$_{TOC}$ signal is dominated by the first order scattering of prevailingly horizontally oriented leaves, lowering the occurrence of fluorescence absorption. The largest multi-angular SIF$_{TOC}$ differences in all tested LAD and LAI scenarios occurred in very oblique viewing angles, in which the modelled radiance is impacted by uncertainties in angular discretization of the upper hemisphere.

Despite of a generally high agreement with SCOPE/mSCOPE simulations, this model cross comparison is not a fully sufficient replacement of an independent validation of the DART model, which is expected to be performed with real canopy SIF$_{TOC}$ measurements in a near future. Nonetheless, this comparison provides the evidence that current integration of the Fluspect model and implementation of the 3D flux-tracking radiative transfer of SIF emitted from geometrically explicit leaves are as plausible as already validated 1D radiative transfer modelling approaches of SCOPE and mSCOPE models (Migliavacca et al., 2017; Pacheco-Labrador et al., 2019; van der Tol et al., 2016; Vilfan et al., 2019). This conclusion provides us with a high level of confidence that the radiative transfer modelling of SIF in DART can be used to investigate the major canopy structural controls of SIF$_{TOC}$ in geometrically explicit 3D canopies, which structural complexity cannot be represented and tested in SCOPE or mSCOPE.

4.2. SIF changes due to classification of sun/shade-adapted leaves and canopy structure

Distinct parametrization of sun- and shade-adapted leaves did not result in major differences in SIF$_{TOC}$, but other canopy structural

parameters were found to be more important. The specific distinction of leaf *fqe* for sun- and shade-adapted foliage appeared to have a smaller impact on DART simulated nadir SIF_{TOC} than increasing LAI and foliage clumping reducing CC from 100% to 50% (c.f., Fig. 1 and Fig. 3). Yet, the impact of the leaf-light adaptation effect might increase, if a DART user applies Q double-threshold values that favour strongly the shade- over the sun-adapted class and simultaneously increases the PSI and PSII *fqe* inputs. Secondly, the influence of the shade-adapted class would be more significant when tested for naturally more clumped and taller (e.g., forest) canopies. Therefore, identification of correct Q thresholds and sun/shade *fqe* values are, together with measurements of canopy gaps and foliage clumping, essential for further investigation of the photosynthetic light adaptations and their impacts on SIF_{TOC}.

When evaluating impacts of maize canopy structural traits, our nadir SIF_{TOC} results indicated a general superior role of LAI over the foliage clumping. However, doubling the foliage clumping of maize crop with LAI = 2 caused such a strong increase in absorption of red SIF photons by chlorophylls that diminished and fully equalled the previous increase in SIF_{TOC} between 650 and 725 nm caused by doubling the number of regularly spaced plants, i.e., twice higher LAI (Fig. 2). Interpretation of DART 3D radiative budget computed for the two SIF local maximums informed us that this strong red SIF reduction took place in the upper half of the canopy (specifically between 50 and 90% of the canopy height; Fig. 7), because the clumping caused a slight enhancement of SIF energy fluxes in most of the lower half canopy parts and the absorption of SIF by soil background was after the clumping introduction lowered. The fact that relative differences of red SIF balances in upper halves of the clumped and unclumped canopies are 2-fold more negative than the same differences of $fAPAR_{green}$ (Fig. 7b) indicates that the increase in foliage shadowing is responsible only for a half of this clumping-induced SIF reduction. The second half is caused by a more frequent recollision and consequent greater absorption of red SIF photons by leaf photosynthetic pigments. Clumping driven results for LAI = 1 showed less consistent and milder effects, which means that canopy must have a certain minimal leaf density to produce these interactions.

Clumping impacts caused by decreasing CC can be also demonstrated on the example of white peppermint stands without woody material. According to results listed in Table 2, decrease of CC from 80% to 40% triggered a reduction in $fAPAR_{green}$ and, consequently, in emitted SIF by 34%, and simultaneously lowered the SIF_{TOC} by 45% at 686 nm and by

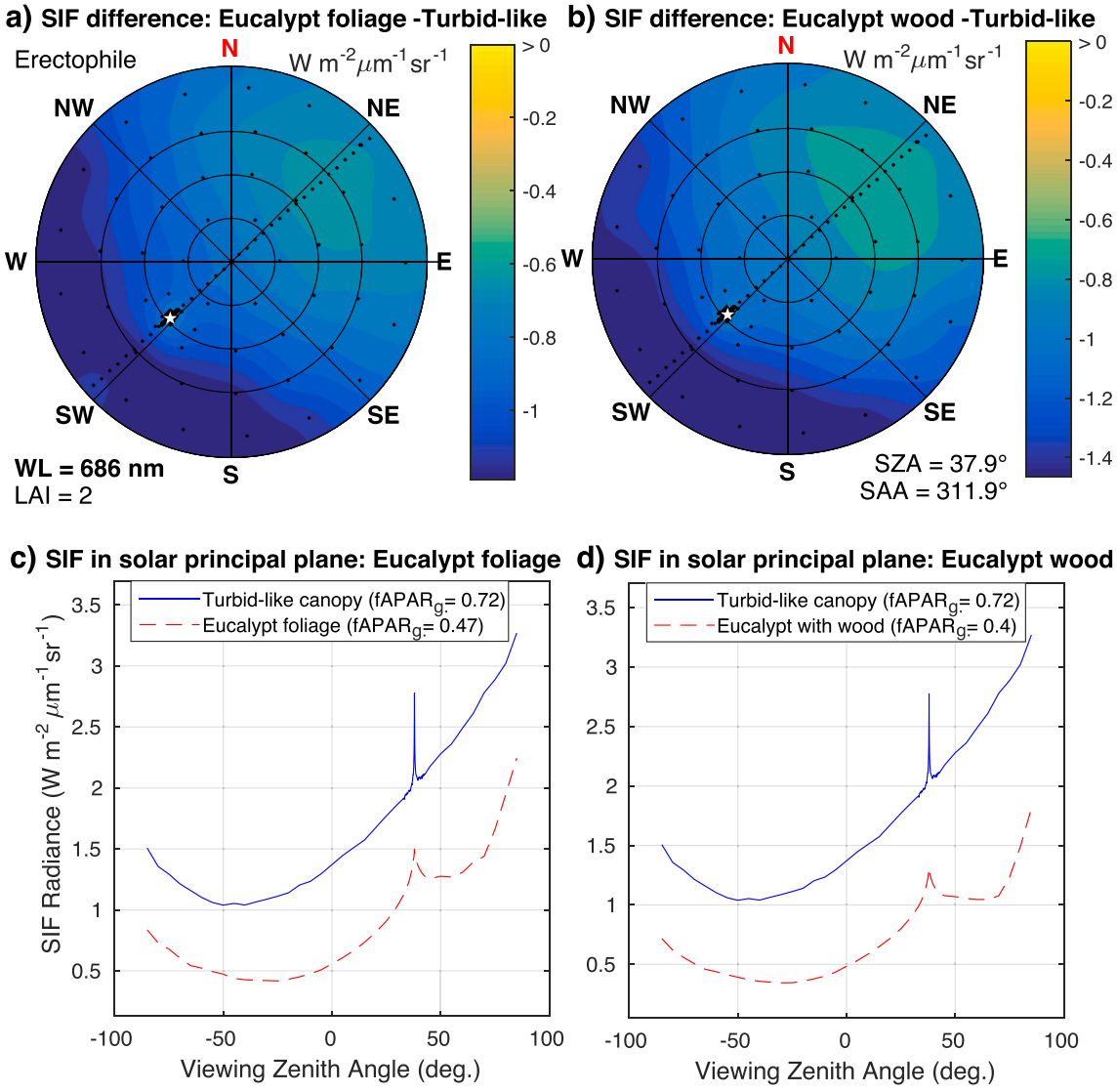

Fig. 8. Multi-angular differences in SIF radiance at 686 nm between a) a dense eucalyptus canopy created only by foliage, b) the same canopy containing also woody components and a DART simulated turbid-like canopy, all with LAI = 2, Erectophile LAD and loamy soil as ground. SIF radiances in the solar principal plane for the turbid-like canopy together with the foliage-only (RMSE = 0.82 and d = 0.55) and the foliage with wood (RMSE = 1.0 and d = 0.47) eucalypt canopies are illustrated in c) and d), respectively (for abbreviations and symbols see Fig. 5).

40% at 740 nm. Thereby, if one accepts an assumption that scattering rates of red and far-red SIF photons by the canopy structures (including structures of a leaf interior without foliar pigments) are equal, then doubling the leaf density while keeping a constant canopy LAI = 2 induced an additional 5% decrease in red SIF_{TOC} attributed to a higher red SIF absorption by chlorophylls. It is important to mention that different quantitative impacts of LAI and foliage clumping on SIF_{TOC} might be revealed if the classification of sun/shade-adapted leaves is included and different (i.e., light adaptation specific) PSI and PSII *fqe* values are specified by a DART user. Since the natural variability in *fqe* and leaf biochemistry was not accounted for in this study, a direct comparison (validation) of these results with SIF observations of real croplands or forests (e.g., Guan et al., 2015; He et al., 2020; Peng et al., 2020; Wang et al., 2020) would be misleading.

Multi-angular DART simulations of SIF_{TOC} demonstrate that the influence of leaf size, foliage angularity and its clumping (CC) is equally or even more crucial for modulating SIF_{TOC} in oblique viewing directions. The polar plots of SIF_{TOC} at 686 nm for maize (Fig. 5b) and eucalyptus (Fig. 8a) canopies with LAI = 2 revealed the largest influence in very oblique backward directions behind the hotspot and the smallest impact in forward directions opposite to the hotspot. The patterns of angular anisotropy for SIF_{TOC} at 740 nm are rather different. A significant impact of maize canopy structure was found around the Northern and the Southern viewing angles (Fig. 6b), whereas only the Southern viewing directions were impacted by the eucalyptus canopy architecture (Fig. 9a). Thus, far-red SIF_{TOC} of each architecturally distinct plant formation (i.e., plant functional type) must be approached individually and the canopy specific structural confounding effects must be removed or at least reduced before any application of remotely sensed SIF_{TOC}. This recommendation is in line with a number of recent works developing far-red SIF_{TOC} normalization approaches to mitigate the canopy structural effects (Liu et al., 2019b; Yang and van der Tol, 2018; Yang et al., 2020b; Zeng et al., 2019).

4.3. Impacts of wood structures on eucalyptus SIF_{TOC} signal and SIF escape factors

Accounting for presence of bark-covered wood structures in our eucalyptus simulations decreased nadir 740 nm SIF_{TOC} by about 23% for the dense canopy and by 13% for the sparse canopy (Table 2). Results

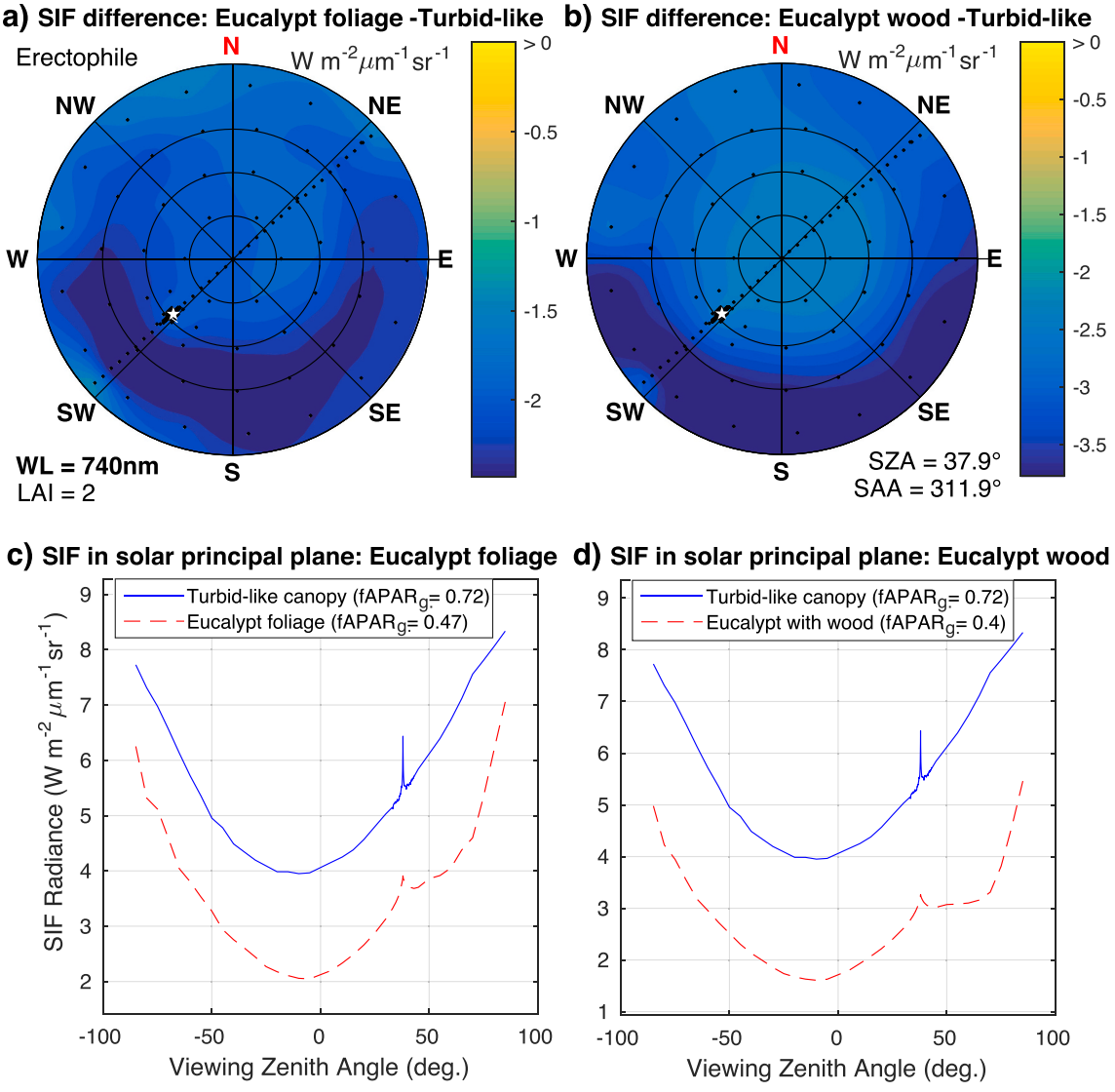

Fig. 9. Multi-angular differences in SIF radiance at 740 nm between a) a dense eucalyptus canopy created only by foliage, b) the same canopy containing also woody components and a DART simulated turbid-like canopy, all with LAI = 2, Erectophile LAD and loamy soil as ground. SIF radiances in the solar principal plane for the turbid-like canopy together with the foliage-only (RMSE = 1.93 and d = 0.47) and the foliage with wood (RMSE = 2.68 and d = 0.35) eucalypt canopies are illustrated in c) and d), respectively (for abbreviations and symbols see Fig. 5).

suggest that approximately one quarter of the total SIF reduction is caused by direct optical interactions (obstruction) of far-red SIF photons with bark surfaces in combination with green leaves under the natural geometrical distributions, whereas three quarters of the reduction resulted from the reduction in $APAR_{green}$ due to wood shadowing. Having the bark reflectance and absorptance at 740 nm both equal to 50%, the wood structures of white peppermint trees acted, on one hand, as strong reflectors and boosted the far-red SIF emission produced in top 25% of the dense canopy (Fig. 10a). On the other hand, they acted as a far-red SIF sink in the rest of the canopy, i.e., in lower 75% of the canopy relative height. Although it is expected that tree species with a lower bark near infrared reflectance will demonstrate radiative budgets with a higher far-red SIF obstruction (absorptance), the consistently decreasing nadir obstruction effects of both modelled eucalyptus stand indicate that the wood obstruction is a regular confounding factor that must be treated as a systematic error source. Therefore, it should be accounted for, or if feasible even corrected, when interpreting far-red SIF_{TOC} data sensed remotely over forests.

The effect of woody material on nadir SIF_{TOC} at 686 nm was smaller, because the total pool of canopy red SIF photons originating just from PSII is naturally small and additionally reduced by absorption of photosynthetic pigments. Interestingly, the bark absorptance of 60% and reflectance of 40% at 686 nm, in combination with the specific geometry of eucalypt tree crowns (i.e., a strong branch foliage clumping with Erectophile LAD), decreased the red SIF nadir escape factor of the sparse canopy by 0.6%, whereas the same SIF escape factor in the dense canopy was increased by 1.5%. If we accept these simulations as generally applicable, we may conclude that the presence of wood affects the red SIF forest canopy balance in both negative and positive ways. However, the impact is generally small, predominantly influencing the less emitting lower 75% of the canopy height rather than larger emissions originating from top 25% of the canopy. Since we modelled and analyzed only two mono-species eucalyptus stands, additional simulations for other tree species, including natural variability in species-specific optical, biochemical and structural properties, will be essential to draw more comprehensive and generic conclusions regarding the wood obstruction effects.

DART estimates of the relative eucalyptus canopy SIF escape factor in the nadir direction, which can be used to compute the apparent SIF efficiency (a gross primary production proxy less impacted by canopy structures; Wang et al., 2020), were quite low, smaller than 0.15 for red and 0.27 for far-red SIF. Nonetheless, the omnidirectional escape factors of individual canopy layers were higher, reaching up to 0.65 for red and 0.9 for far-red SIF in the highly emissive top 25% of the canopy height (Fig. 10b). These numbers and results in Figs. 9 and 10 suggest that oblique multi-directional observations of forest canopies (e.g., with tower-based instruments) should capture more SIF photons than a single nadir measurement, and, thus, provide a stronger SIF_{TOC} signal. Once again, more simulations covering different forest types and their natural variability are required to conclude if these interpretations have a general applicability or if the white peppermint canopies represent a unique and possibly extreme case.. Despite a limited size of this study, we demonstrate that the entire 3D structural complexity, including woody material, must be taken into account when assessing quantity of SIF photons scattered and absorbed by canopy components and those escaping from a forest canopy.

4.4. Development of DART SIF modelling for large canopies and landscapes

DART SIF simulations for geometrically explicit representations of terrestrial vegetation have computational limitations regarding a simulated scene size and a number of objects (i.e., triangular facets) creating 3D mock-ups of plant canopies. Theoretically, one can create an extensive landscape occupied with an unlimited population of plants and other 3D objects (e.g., open-water bodies, roads, buildings, etc.), but the SIF simulation, and mainly radiative budget, of such a scene might be practically unfeasible as the computer memory and processor capabilities are not unlimited. Therefore, another two approaches, allowing more efficient simulations of large canopies and extensive landscapes, are being implemented and tested in DART: i) SIF modelling for vegetation canopies represented by 3D turbid voxels (i.e., voxels filled with a vegetation turbid medium), and ii) a direct and reverse MC modelling called DART-Lux (Gastellu-Etchegorry et al., 2020). The latter one is especially highly promising for simulating extensive SIF_{TOC} images. It uses only the landscape elements contributing to the formation of a simulated image, which decreases the computer time and memory by a factor as large as 100. Once fully tested and solidified, both approaches

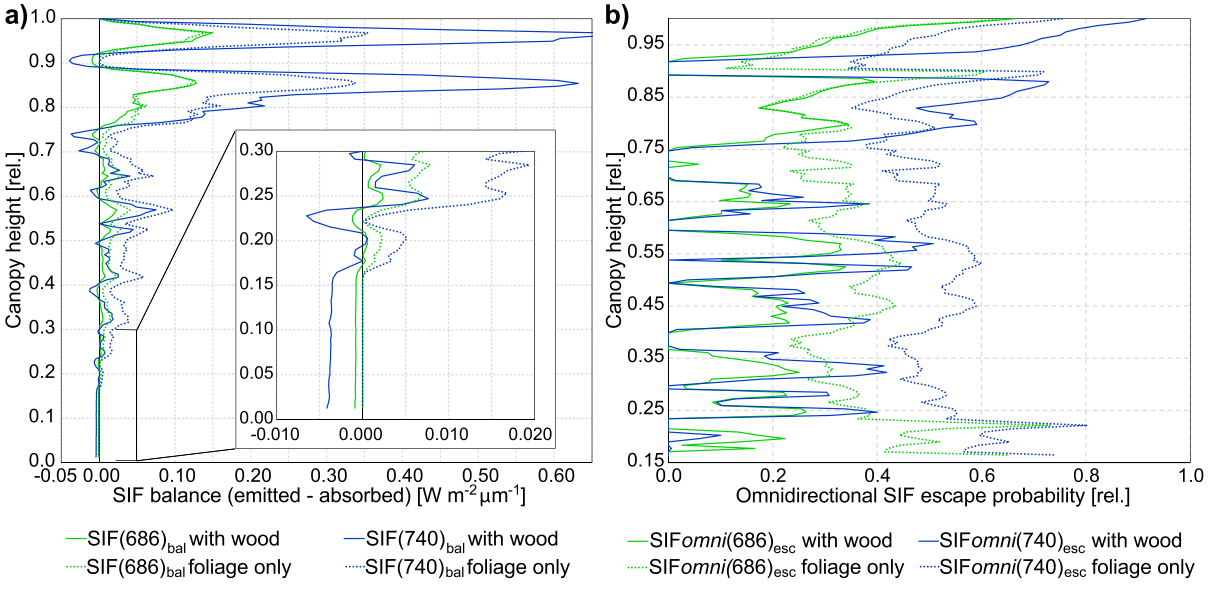

Fig. 10. Vertical profiles of a) SIF balances ($SIF(\lambda)_{bal}$) and b) relative omnidirectional SIF escape factors ($SIFomni(\lambda)_{esc}$) at 686 and 740 nm for a dense white peppermint (*Eucalyptus pulchella*) canopy (CC ≈ 80% and LAI = 2) created only by foliage (dashed lines) and the same canopy containing also woody components (solid lines). Each 10 cm thick canopy layer is presented as a point of the relative canopy height [0–1]. For details about computations of $SIF(\lambda)_{bal}$ and $SIFomni(\lambda)_{esc}$ see Section 2.4.

will provide DART users with potential satellite SIF observations adapted to common ground sampling distances of hundreds of meters. Such simulations could test multiple SIF confounding optical effects, for instance, those originating from photosynthetically inactive Earth surfaces of rough terrain configurations resulting in dynamic spatiotemporal irradiation changes and shadow patterns.

5. Conclusions

Physical and technical implementation of discrete anisotropic radiative transfer modelling for solar-induced chlorophyll fluorescence in geometrically explicit 3D plant canopies was described and compared with complementary cases simulated in 1D models SCOPE and mSCOPE. The cross-comparison revealed that DART simulations of SIF_{TOC} for geometrically simple and spatially homogenous canopies produced nearly the same results as both 1D models. The largest SIF_{TOC} differences occurred in very oblique viewing angles that are impacted by higher modelling uncertainties than the directions closer to nadir.

Further exploitation of DART ability to simulate SIF images and radiative budgets of virtual 3D maize crops showed that the distinction and adjustment of fluorescence efficiencies for sun- and shade-adapted leaves had a smaller impact on DART simulated SIF_{TOC} than an increase in leaf density (LAI) and local foliage clumping. When analysing nadir SIF_{TOC} impacts by foliar density traits, we found a superior role of LAI over the foliage clumping. Nonetheless, the foliage clumping was shown to be an important controlling factor of maize and eucalyptus SIF_{TOC} simulated at 686 and 740 nm in oblique viewing directions, and also a crucial driver of the red SIF balance, i.e., SIF emission and absorption, in vertical profile of irregularly spaced maize crop with LAI = 2. These study outcomes must be, however, reproduced for other plant functional types to confirm and investigate further the influences of leaf light intensity adaptations and density traits on SIF variability inside and at the top of different canopies.

DART simulations of two white peppermint eucalyptus stands suggested that woody material has a significant impact on SIF_{TOC}. Trunks and branches cast shadows on photosynthesizing leaves, decreasing their SIF emissions by about 15% in dense and 8% in sparse canopy simulations. Although the absorbance and reflectance of eucalyptus bark (both about 50% at 740 nm), in combination with a multiple scattering and absorption by leaves, nearly doubled the pool of far-red SIF photons in the top 25% part of dense canopy, they reduced the overall canopy escape of far-red SIF in the nadir viewing direction by 6% and 4% in the sparse stand. Interestingly, the nadir escape factors of red SIF from dense and sparse canopies were almost unimpacted by presence of woody material, despite a relatively high 40% reflectance of bark at 686 nm. These unique results demonstrate that further development of SIF 3D radiative transfer modelling has a potential to reveal new insights in SIF observations of spectrally, spatially and topographically heterogeneous vegetated landscapes, acquired at different spatial scales by proximal, airborne and space-borne optical sensors.

Author statement

ZM, OR, TY and JPGE prepared methodological design of the study based on the original idea conceived by ZM, JPGE, DM and BDC. OR, ND, PY, CT and JPGE carried out and analyzed the SCOPE and mSCOPE modelling of turbid medium vegetation simulations. ZM, TY, AD, JM and GM conducted and analyzed the DART model simulations for turbid-like medium and maize canopies. RJ and ZM executed and analyzed the DART simulations of white peppermint forest stands. NL, JG, TY, EC and OR and were responsible for implementation and programming of solar-induced radiative transfer algorithm in DART. NL, JG, ZM, CT and PY were involved in the DART implementation and programming of the Fluspect leaf model. All authors co-wrote the first version of the manuscript, and ZM, OR, TY, JPGE, DM and BDC were responsible for final synthesis, revision and corrections of the manuscript.

Declaration of Competing Interest

None.

Acknowledgments

Authors are grateful to Luke Wallace and Samuel Hillman from the RMIT University in Melbourne for acquisition and pre-processing of TLS point clouds of the white peppermint eucalypt trees, permitting their 3D virtual constructions. We also acknowledge constructive reviews of the anonymous peers that helped us to improve scientific quality and readability of this manuscript. Contribution of Z. Malenovský was funded by the NASA Earth Science Division (ESD) in support of the 'FLuorescence Airborne Research Experiment (FLARE)' and by the Australian Research Council Future Fellowship 'Bridging Scales in Remote Sensing of Vegetation Stress' (FT160100477). Contribution of the CESBIO Laboratory authors was supported by the TOSCA project 'Fluo3D' and by the PhD program of the French Space Center (CNES) and the Centre National de Recherche Scientifique (CNRS). Work of R. Janoutová was supported by the Ministry of Education, Youth and Sports of CR within the CzeCOS program (grant LM2018123). Involvement of P. Yang was supported by the Netherlands Organization for Scientific Research (grant ALWGO.2017.018).

Appendix A. Comparison of DART and SCOPE/mSCOPE SIF radiative transfers

Since SCOPE and mSCOPE are turbid medium models, we prepared DART 3D simulations mimicking their 1D canopies as closely as possible. SCOPE, mSCOPE and DART were adjusted to use the same bottom-of-atmosphere (BOA) solar direct and diffuse irradiance, simulated with DART atmosphere radiative transfer module using the United States standard atmosphere gas model (NOAA, NASA, and Air-Force, U.S, 1976) and the rural area aerosol model with a visibility of 23 km. The scene was a 1 m height vegetation canopy above a bare soil with three Lambertian reflectance (ρ) properties: i) black soil ($\rho = 0$), ii) half-reflective soil ($\rho = 0.5$), and iii) loamy gravel brown dark soil with ρ linearly increasing with wavelength ($\rho \approx$ 6% at 550 nm, $\rho \approx 12\%$ at 686 nm and $\rho \approx 15\%$ at 740 nm). Every leaf facet had the same specific Lambertian reflectance and transmittance, i.e., there was no division of leaf optical properties on sunlit or sun-adapted and shaded or shade-adapted leaves. The Fluspect leaf SIF matrices (M_{xyij}; Eqn 1) were implemented in DART exactly as in SCOPE v. 1.62, using the same units for radiation fluxes. Their improved implementation, introduced in SCOPE v. 2.1, leads to different results and it is included in DART 5.7.3 from v. 1201 onward. For the DART-SCOPE comparison, the *eta* fluorescence weight parameters were forced to one. For the DART-mSCOPE comparison, we split turbid scenes into two and three almost equally high layers (see Fig. A1ab). Leaves of 2- and 3-layer simulations were divided into sunlit and shaded (see % of sunlit leaves in each layer in Fig. A1cd) and the *eta* parameters simulated per layer for both leaf cohorts in mSCOPE were entered in the corresponding DART simulations. Leaf optical properties were simulated with the same Fluspect version, using the input parameters listed in Table A1. In attempt to simulate strong SIF_{TOC} signals, the *fqe* values for PSI and PSII were selected close to their potential maximums. Simulations considered three leaf densities, specified by the leaf area index (LAI) equal to 1, 2 and 4. In SCOPE simulations, we tested three leaf angle distributions (LAD): Spherical, Erectophile and Planophile (Danson, 1998), whereas we applied only the Spherical function, the most frequent naturally occurring LAD, in mSCOPE simulations. All leaves were homogenously distributed

throughout the canopies, i.e. the foliage clumping index (Chen and Black, 1992) was equal to 1. The DART leaf facets were equilateral triangles with the surface area of 0.08 cm^2. Such small leaf area ensured independency of DART simulated TOC reflectance and SIF from the solar azimuth angle. The leaf width required for SCOPE/mSCOPE computations in the hot-spot direction was set to the height of DART facets, i.e., 0.37 cm. The solar azimuth angle (SAA) was fixed to 311.89° (anticlockwise from South) and the solar zenith angle (SZA) to 37.94° (i.e., solar elevation angle of 52.06°) as for Washington D.C. (USA) area (the Beltsville Agricultural Research Center; Lat. 39.03°N, Long. 76.85°W) on 26th August 2014 at 14.00 local time (i.e., at 13.50 solar time). Nadir SIF_{TOC} radiance [$W.m^{-2}.\mu m^{-1}.sr^{-1}$] between 640 and 850 nm (1 nm bandwidth) was simulated for all combinations of the input parameters with the three RTMs. The obtained PSI, PSII and total SIF_{TOC} values were compared statistically (as described in Section 2.6).

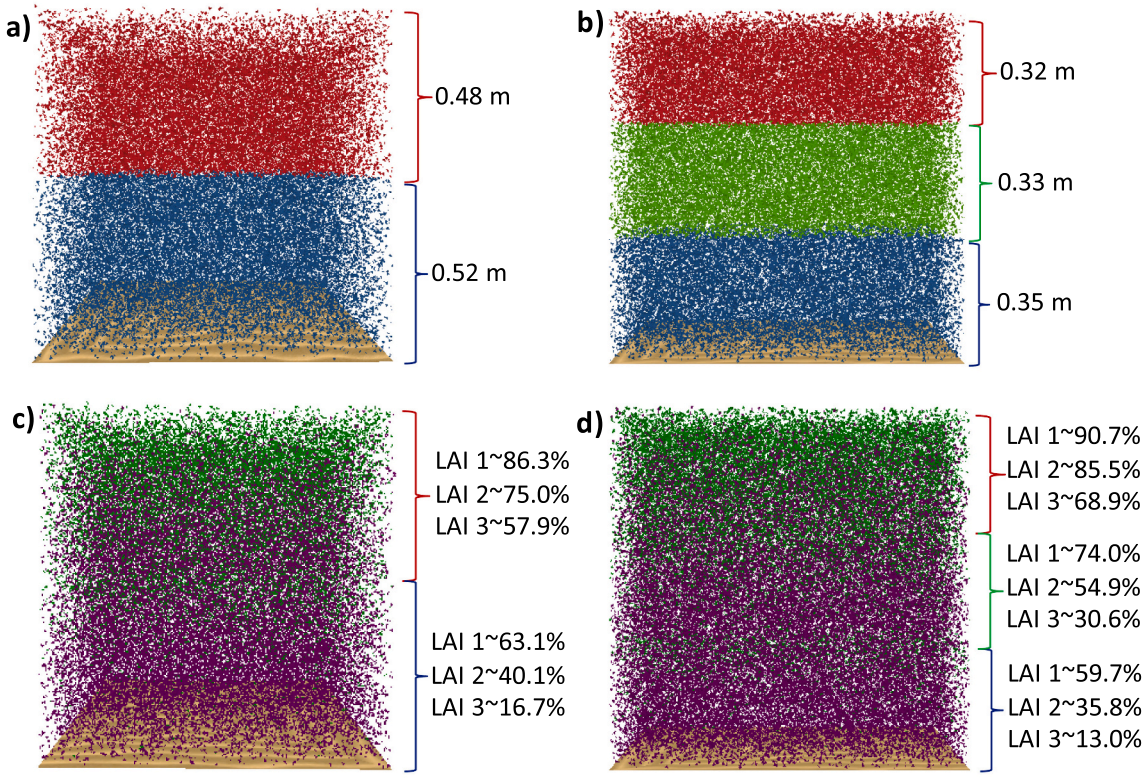

Fig. A1. DART representations of a) 2- and b) 3-layered turbid-like canopies designed for comparison with the mSCOPE model (numbers indicate the height of each layer). Illustration of sunlit (under direct illumination; green) and shaded (under diffuse illumination, violet) triangular leaves for both c) 2- and d) 3-layered canopies (numbers indicate % of sunlit leaves per layer for each simulated LAI). (For interpretation of the references to colour in this figure legend, the reader is referred to the web version of this article.)

Table A1
Input parameters of the Fluspect model used to simulate optical properties of SCOPE/mSCOPE turbid medium leaves and corresponding DART leaves (for explanations of input abbreviations see caption of Table 1).

Fluspect inputs (m)SCOPE layers	Cab [$\mu g.cm^{-2}$]	Car [$\mu g.cm^{-2}$]	EWT [cm]	LMA [$g.cm^{-2}$]	N	PSI *fqe*	PSII *fqe*
mSCOPE first layer (from top)	40	10	0.006	0.0014	1.0	0.006	0.03
SCOPE & mSCOPE second layer	60	15	0.009	0.0021	1.5	0.006	0.03
mSCOPE third layer (from top)	80	20	0.012	0.0028	2	0.006	0.03

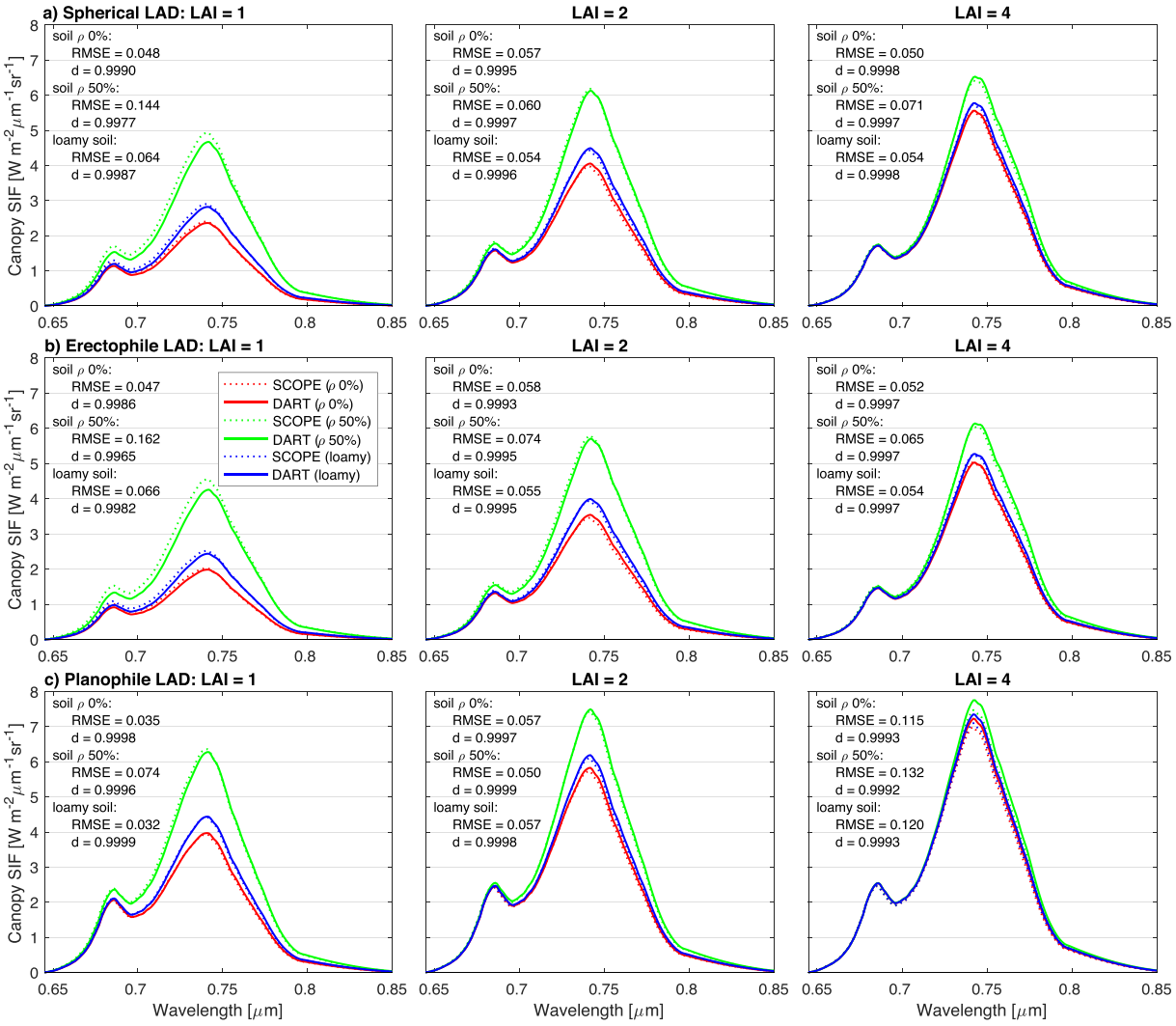

Fig. A2. DART and SCOPE total nadir SIF of vegetation canopies with LAI = 1, 2 and 4, three soils (ρ = 0%, ρ = 50%, ρ = loamy dark gravel soil), and with a) Spherical, b) Erectophile, and c) Planophile LAD (RMSE ~ root mean square error; d ~ index of agreement: 0 = no agreement, 1 = full agreement).

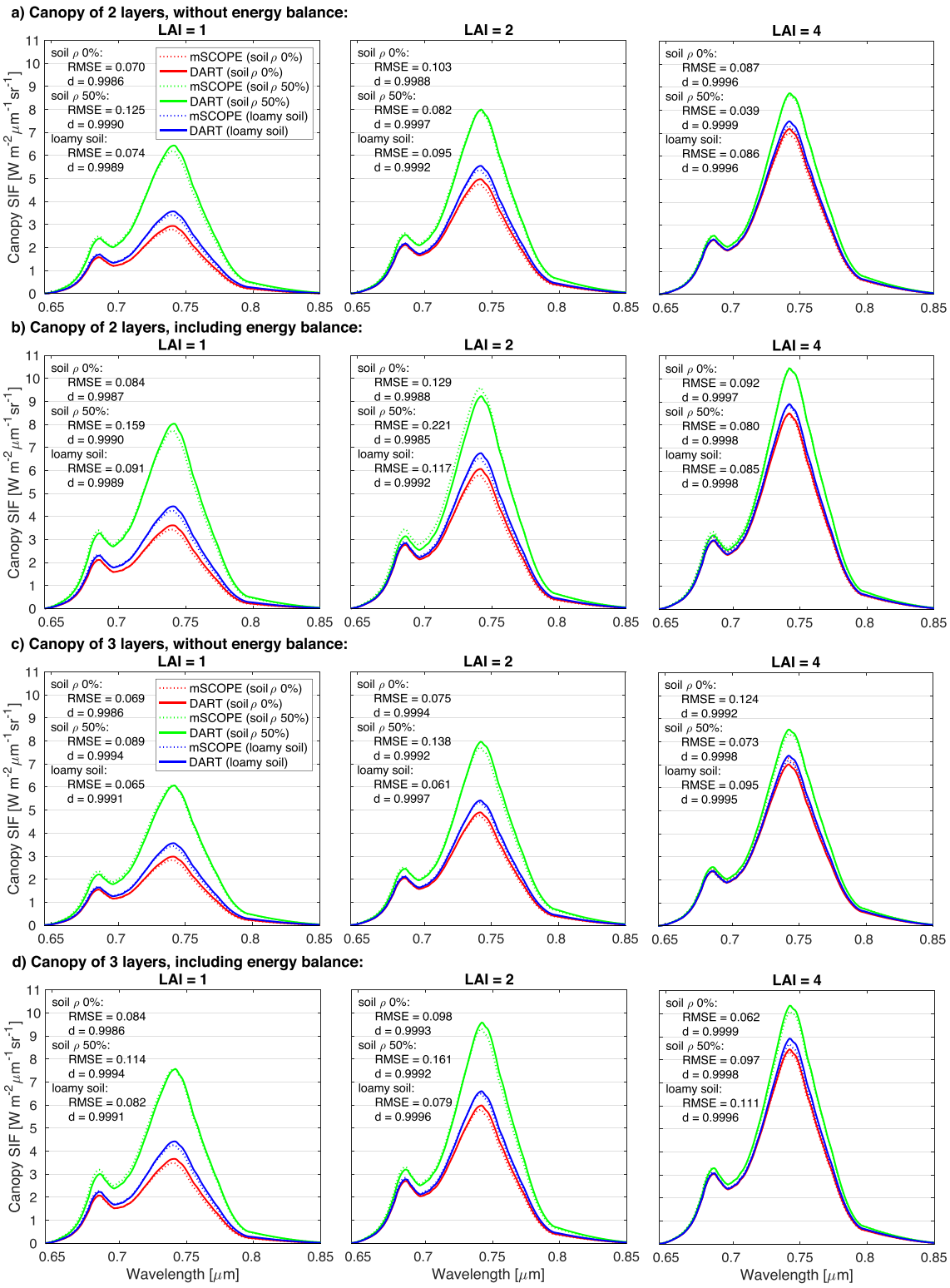

Fig. A3. DART and mSCOPE nadir SIF of vegetation canopies simulated with the Spherical LAD, three soils (ρ = 0%, ρ = 50%, ρ = loamy dark gravel soil) in two layers a) without and b) with energy balance, and in three layers c) without and d) with energy balance (for abbreviations see Fig. A2).

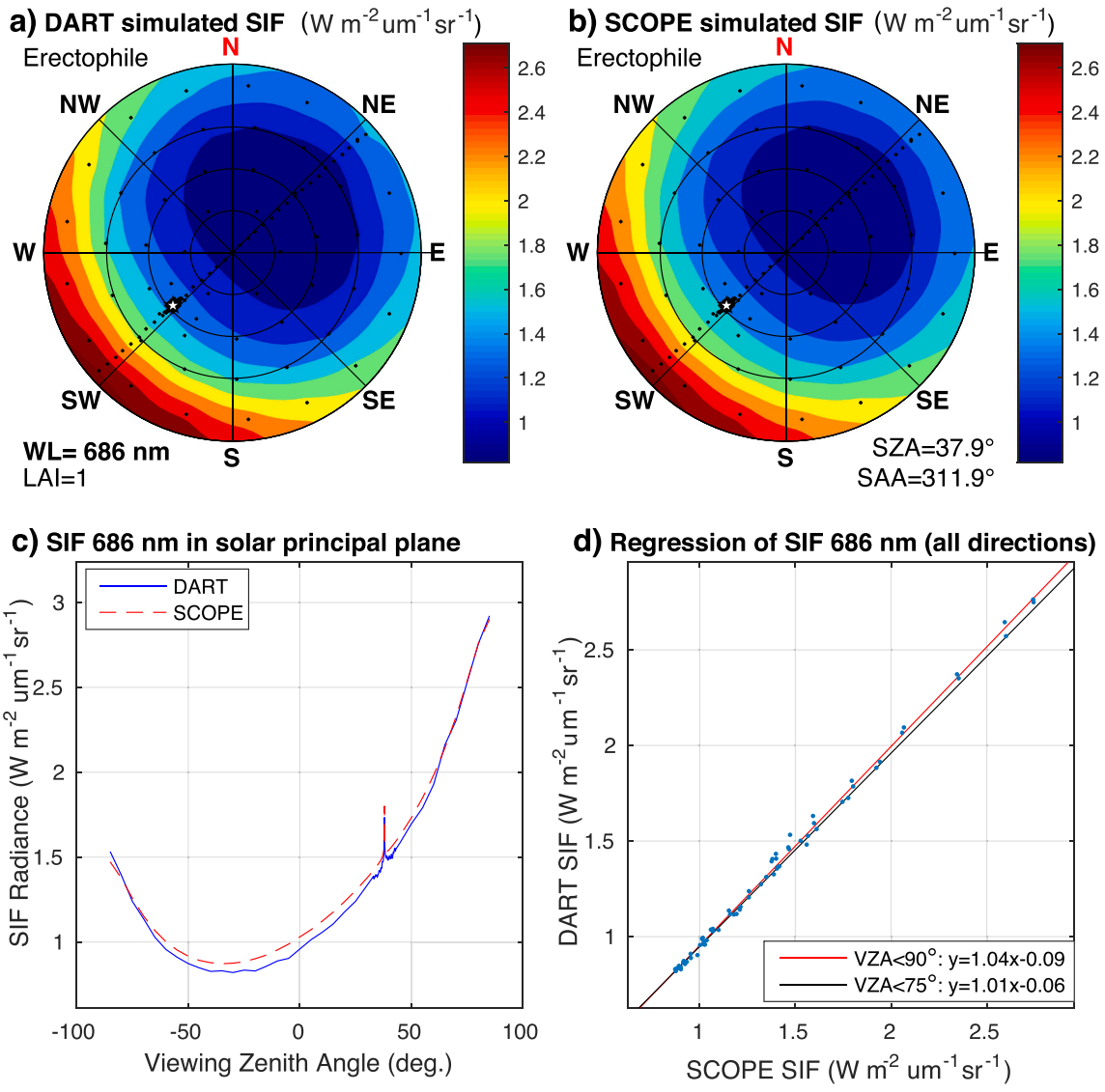

Fig. A4. Best agreement when comparing a) DART and b) SCOPE multi-angular SIF of a turbid medium canopy was found for the Erectophile LAD and a null soil reflectance. SIF radiance in the solar principal plane and linear regression of turbid-like DART and turbid SCOPE simulations ($R^2 = 0.99$, RMSE = 0.03, d = 1.0 for all simulated viewing directions, i.e., VZA < 90°, and RMSE = 0.02 for VZA < 75°) are shown in c) and d) graphs, respectively (for abbreviations and symbols see Fig. 5).

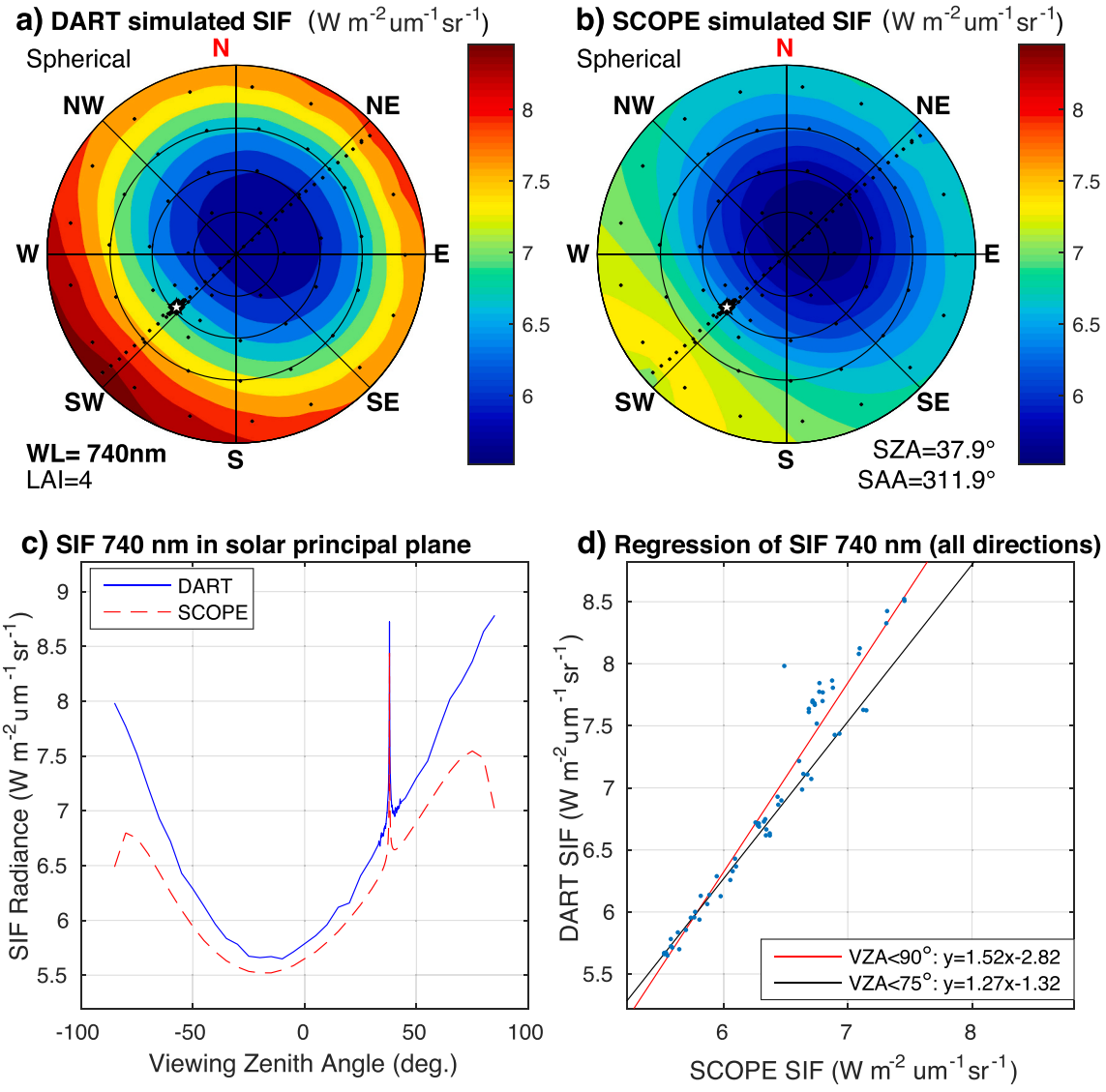

Fig. A5. Worst agreement when comparing a) DART and b) SCOPE multi-angular SIF of turbid medium canopy with the Spherical LAD and a 50% reflective soil. SIF radiance in the solar principal plane and linear regression of turbid-like DART and turbid SCOPE simulations ($R^2 = 0.94$, RMSE = 0.21, d = 1.0 for VZA < 90° and $R^2 = 0.99$, RMSE = 0.07 for VZA < 75°) are shown in c) and d) graphs, respectively (for abbreviations and symbols see Fig. 5).

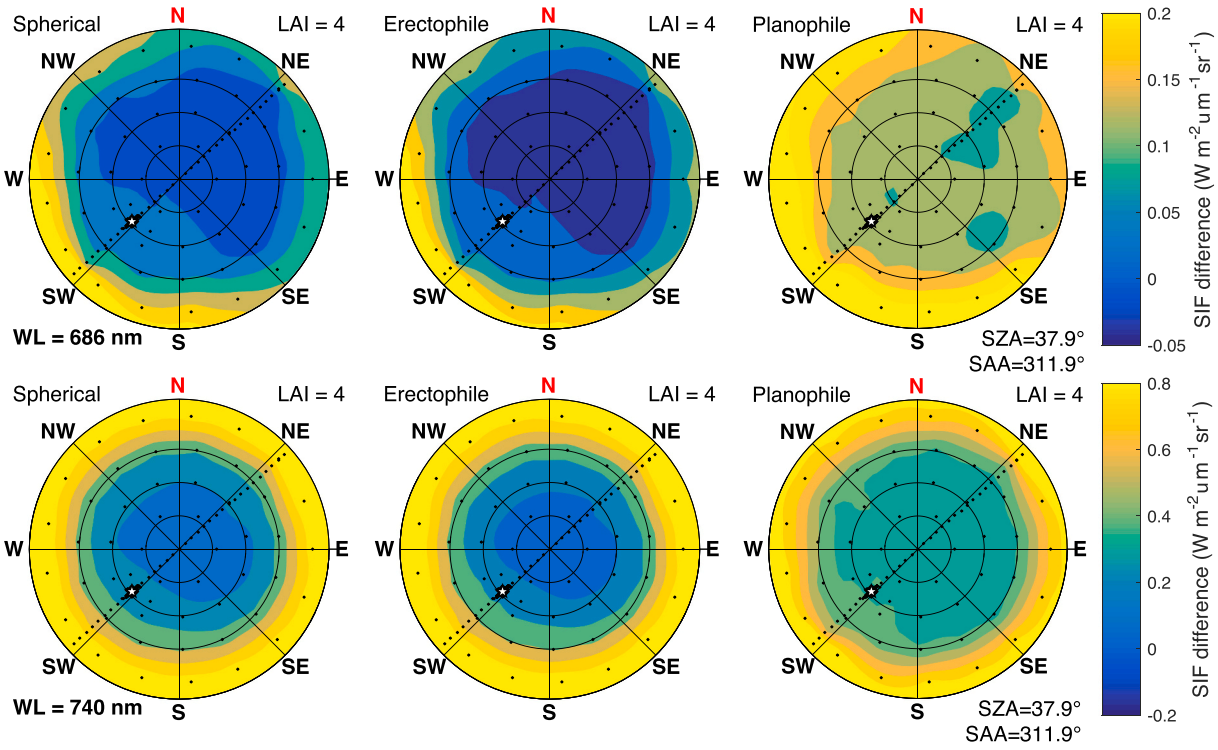

Fig. A6. DART–SCOPE differences in multi-angular SIF radiance at 686 and 740 nm for a canopy with LAI = 4, having Spherical, Erectophile and Planophile LADs (the white star shows the solar position and black dots indicate the simulated viewing directions; for abbreviations see Fig. 5).

References

Aasen, H., Van Wittenberghe, S., Sabater Medina, N., Damm, A., Goulas, Y., Wieneke, S., Hueni, A., Malenovský, Z., Alonso, L., Pacheco-Labrador, J., Cendrero-Mateo, P.M., Tomelleri, E., Burkart, A., Cogliati, S., Rascher, U., Mac Arthur, A., 2019. Sun-induced chlorophyll fluorescence II: review of passive measurement setups, protocols, and their application at the leaf to canopy level. Remote Sens. 11, 927.

Ashley, M.D., Rea, J., 1975. Seasonal vegetation differences from ERTS imagery. Journal of American Society of Photogrammetry 41, 713–719.

Bendig, J., Malenovský, Z., Gautam, D., Lucieer, A., 2020. Solar-induced chlorophyll fluorescence measured from an unmanned aircraft system: sensor Etaloning and platform motion correction. IEEE Trans. Geosci. Remote Sens. 58, 3437–3444.

Blair, B.O., Baumgardner, M.F., 1977. Detection of the green and Brown wave in hardwood canopy covers using multidate, multispectral data from LANDSAT-11. Agron. J. 69, 808–811.

Blender, 2007. https://www.blender.org/ (12 February 2020).

Chen, J.M., Black, T.A., 1992. Defining leaf area index for non-flat leaves. Plant Cell Environ. 15, 421–429.

Croft, H., Chen, J.M., Wang, R., Mo, G., Luo, S., Luo, X., He, L., Gonsamo, A., Arabian, J., Zhang, Y., Simic-Milas, A., Noland, T.L., He, Y., Homolová, L., Malenovský, Z., Yi, Q., Beringer, J., Amiri, R., Hutley, L., Arellano, P., Stahl, C., Bonal, D., 2020. The global distribution of leaf chlorophyll content. Remote Sens. Environ. 236, 111479.

Danson, F.M., 1998. Teaching the physical principles of vegetation canopy reflectance using the SAIL model. In: Photogrammetric Engineering & Remote Sensing, *64*, pp. 809–812.

DART, 2019. https://dart.omp.eu/Public/documentation/contenu/documentation/DART_handbook.pdf (6 February 2020).

DART, 2020. https://dart.omp.eu/Public/documentation/contenu/documentation/DART_User_Manual.pdf (6 February 2020).

Féret, J.B., Berger, K., de Boissieu, F., Malenovský, Z., 2021. PROSPECT-PRO for estimating content of nitrogen-containing leaf proteins and other carbon-based constituent. Remote Sens. Environ. 252, 112173.

Féret, J.B., Gitelson, A.A., Noble, S.D., Jacquemoud, S., 2017. PROSPECT-D: towards modeling leaf optical properties through a complete lifecycle. Remote Sens. Environ. 193, 204–215.

Frankenberg, C., Butz, A., Toon, G.C., 2011. Disentangling chlorophyll fluorescence from atmospheric scattering effects in O2 A-band spectra of reflected sun-light. Geophysical Research Letters 38.

Gamon, J.A., Somers, B., Malenovský, Z., Middleton, E.M., Rascher, U., Schaepman, M. E., 2019. Assessing vegetation function with imaging spectroscopy. Surv. Geophys. 40, 489–513.

Gastellu-Etchegorry, J.P., 2008. 3D modeling of satellite spectral images, radiation budget and energy budget of urban landscapes. Meteorog. Atmos. Phys. 102, 187.

Gastellu-Etchegorry, J.P., Demarez, V., Pinel, V., Zagolski, F., 1996. Modeling radiative transfer in heterogeneous 3-D vegetation canopies. Remote Sens. Environ. 58, 131–156.

Gastellu-Etchegorry, J.P., Martin, E., Gascon, F., 2004. DART: a 3D model for simulating satellite images and studying surface radiation budget. Int. J. Remote Sens. 25, 73–96.

Gastellu-Etchegorry, J.-P., Yin, T., Lauret, N., Cajgfinger, T., Gregoire, T., Grau, E., Feret, J.-B., Lopes, M., Guilleux, J., Dedieu, G., Malenovský, Z., Cook, B., Morton, D., Rubio, J., Durrieu, S., Cazanave, G., Martin, E., Ristorcelli, T., 2015. Discrete anisotropic Radiative transfer (DART 5) for modeling airborne and satellite Spectroradiometer and LIDAR acquisitions of natural and urban landscapes. Remote Sens. 7, 1667–1701.

Gastellu-Etchegorry, J.P., Lauret, N., Yin, T., Landier, L., Kallel, A., Malenovský, Z., Bitar, A.A., Aval, J., Benhmida, S., Qi, J., Medjdoub, G., Guilleux, J., Chavanon, E., Cook, B., Morton, D., Chrysoulakis, N., Mitraka, Z., 2017. DART: recent advances in remote sensing data modeling with atmosphere, polarization, and chlorophyll fluorescence. IEEE Journal of Selected Topics in Applied Earth Observations and Remote Sensing 10, 2640–2649.

Gastellu-Etchegorry, J.-P., Wang, Y., Regaieg, O., Yin, T., Malenovský, Z., Zhen, Z., Yang, X., Tao, Z., Landier, L., Al Bitar, A., Deschamps, A., Lauret, N., Guilleux, J., Chavanon, E., Cao, B., Qi, J., Kallel, A., Mitraka, Z., Chrysoulakis, N., Cook, B., Morton, D., 2020. Recent improvements in the DART model for atmosphere, topography, large landscape, chlorophyll fluorescence, satellite image inversion. In: IEEE International Geoscience and Remote Sensing Symposium (p. 5). Virtual Symposium. IEEE.

Givnish, T.J., 1988. Adaptation to Sun and shade: a whole-plant perspective. Funct. Plant Biol. 15, 63–92.

Guan, K., Pan, M., Li, H., Wolf, A., Wu, J., Medvigy, D., Caylor, K.K., Sheffield, J., Wood, E.F., Malhi, Y., Liang, M., Kimball, J.S., Saleska, Scott R., Berry, J., Joiner, J., Lyapustin, A.I., 2015. Photosynthetic seasonality of global tropical forests constrained by hydroclimate. Nat. Geosci. 8, 284–289.

Guanter, L., Alonso, L., Gómez-Chova, L., Amorós-López, J., Vila, J., Moreno, J., 2007. Estimation of solar-induced vegetation fluorescence from space measurements. Geophysical Research Letters 34.

Guanter, L., Zhang, Y., Jung, M., Joiner, J., Voigt, M., Berry, J.A., Frankenberg, C., Huete, A.R., Zarco-Tejada, P., Lee, J.-E., Moran, M.S., Ponce-Campos, G., Beer, C., Camps-Valls, G., Buchmann, N., Gianelle, D., Klumpp, K., Cescatti, A., Baker, J.M., Griffis, T.J., 2014. Global and time-resolved monitoring of crop photosynthesis with chlorophyll fluorescence. Proceedings of the National Academy of Sciences *111*, E1327–E1333.

He, L., Chen, J.M., Liu, J., Mo, G., Joiner, J., 2017. Angular normalization of GOME-2 Sun-induced chlorophyll fluorescence observation as a better proxy of vegetation productivity. Geophys. Res. Lett. 44, 5691–5699.

He, L., Magney, T., Dutta, D., Yin, Y., Köhler, P., Grossmann, K., Stutz, J., Dold, C., Hatfield, J., Guan, K., Peng, B., Frankenberg, C., 2020. From the ground to space: using solar-induced chlorophyll fluorescence to estimate crop productivity. Geophysical Research Letters *47* (e2020GL087474).
Hernández-Clemente, R., North, P.R.J., Hornero, A., Zarco-Tejada, P.J., 2017. Assessing the effects of forest health on sun-induced chlorophyll fluorescence using the FluorFLIGHT 3-D radiative transfer model to account for forest structure. Remote Sens. Environ. 193, 165–179.
Hosgood, B., Jacquemoud, S., Andreoli, G., Verdebout, J., Pedrini, A., Schmuck, G., 1994. Leaf Optical properties experiment 93 (LOPEX93). In: European Commission No. EUR 16095 EN. Joint Research Centre, Institute for Remote Sensing Applications.
Jacquemoud, S., Baret, F., 1990. PROSPECT: a model of leaf optical properties spectra. Remote Sens. Environ. 34, 75–91.
Janoutová, R., Homolová, L., Malenovský, Z., Hanuš, J., Lauret, N., Gastellu-Etchegorry, J.-P., 2019. Influence of 3D spruce tree representation on accuracy of airborne and satellite Forest reflectance simulated in DART. Forests 10, 292.
Joiner, J., Yoshida, Y., Vasilkov, A.P., Yoshida, Y., Corp, L.A., Middleton, E.M., 2011. First observations of global and seasonal terrestrial chlorophyll fluorescence from space. Biogeosciences 8, 637–651.
Kallel, A., 2020. FluLCVRT: reflectance and fluorescence of leaf and canopy modeling based on Monte Carlo vector radiative transfer simulation. J. Quant. Spectrosc. Radiat. Transf. 253, 107183.
Kallel, A., Nilson, T., 2013. Revisiting the vegetation hot spot modeling: case of Poisson/binomial leaf distributions. Remote Sens. Environ. 130, 188–204.
Köhler, P., Guanter, L., Kobayashi, H., Walther, S., Yang, W., 2018. Assessing the potential of sun-induced fluorescence and the canopy scattering coefficient to track large-scale vegetation dynamics in Amazon forests. Remote Sens. Environ. 204, 769–785.
Leuning, R., Kelliher, F.M., De Pury, D.G.G., Schulze, E.D., 1995. Leaf nitrogen, photosynthesis, conductance and transpiration: scaling from leaves to canopies. Plant Cell Environ. 18, 1183–1200.
Liu, W., Atherton, J., Mõttus, M., Gastellu-Etchegorry, J.-P., Malenovský, Z., Raumonen, P., Åkerblom, M., Mäkipää, R., Porcar-Castell, A., 2019a. Simulating solar-induced chlorophyll fluorescence in a boreal forest stand reconstructed from terrestrial laser scanning measurements. Remote Sens. Environ. 232, 111274.
Liu, X., Guanter, L., Liu, L., Damm, A., Malenovský, Z., Rascher, U., Peng, D., Du, S., Gastellu-Etchegorry, J.-P., 2019b. Downscaling of solar-induced chlorophyll fluorescence from canopy level to photosystem level using a random forest model. Remote Sens. Environ. 231, 110772.
Malenovský, Z., Ufer, C., Lhoták̀ová, Z., Clevers, J.G.P.W., Schaepman, M.E., Albrechtová, J., Cudlín, P., 2006. A New Hyperspectral Index for Chlorophyll Estimation of a Forest Canopy: Area under Curve Normalised to Maximal Band Depth between 650–725 Nm. EARSeL eProceedings 5, 161–172.
Malenovský, Z., Martin, E., Homolová, L., Gastellu-Etchegory, J.-P., Zurita-Milla, R., Schaepman, M.E., Pokorný, R., Clevers, J.G.P.W., Cudlín, P., 2008. Influence of woody elements of a Norway spruce canopy on nadir reflectance simulated by the DART model at very high spatial resolution. Remote Sens. Environ. 112, 1–18.
Malenovský, Z., Homolová, L., Zurita-Milla, R., Lukeš, P., Kaplan, V., Hanuš, J., Gastellu-Etchegorry, J.-P., Schaepman, M.E., 2013. Retrieval of spruce leaf chlorophyll content from airborne image data using continuum removal and radiative transfer. Remote Sens. Environ. 131, 85–102.
Malenovský, Z., Homolová, L., Lukeš, P., Buddenbaum, H., Verrelst, J., Alonso, L., Schaepman, M.E., Lauret, N., Gastellu-Etchegorry, J.-P., 2019. Variability and uncertainty challenges in scaling imaging spectroscopy retrievals and validations from leaves up to vegetation canopies. Surv. Geophys. 40, 631–656.
Migliavacca, M., Perez-Priego, O., Rossini, M., El-Madany, T.S., Moreno, G., van der Tol, C., Rascher, U., Berninger, A., Bessenbacher, V., Burkart, A., Carrara, A., Fava, F., Guan, J.H., Hammer, T.W., Henkel, K., Juarez-Alcalde, E., Julitta, T., Kolle, O., Martín, M.P., Musavi, T., Pacheco-Labrador, J., Pérez-Burgueño, A., Wutzler, T., Zaehle, S., Reichstein, M., 2017. Plant functional traits and canopy structure control the relationship between photosynthetic CO2 uptake and far-red sun-induced fluorescence in a Mediterranean grassland under different nutrient availability. New Phytol. 214, 1078–1091.
Mohammed, G.H., Colombo, R., Middleton, E.M., Rascher, U., van der Tol, C., Nedbal, L., Goulas, Y., Pérez-Priego, O., Damm, A., Meroni, M., Joiner, J., Cogliati, S., Verhoef, W., Malenovský, Z., Gastellu-Etchegorry, J.-P., Miller, J.R., Guanter, L., Moreno, J., Moya, I., Berry, J.A., Frankenberg, C., Zarco-Tejada, P.J., 2019. Remote sensing of solar-induced chlorophyll fluorescence (SIF) in vegetation: 50 years of progress. Remote Sens. Environ. 231, 111177.
Myneni, R.B., Ross, J., 2012. Photon-Vegetation Interactions: Applications in Optical Remote Sensing and Plant Ecology. Springer, Berlin Heidelberg.
Niinemets, Ü., Keenan, T.F., Hallik, L., 2015. A worldwide analysis of within-canopy variations in leaf structural, chemical and physiological traits across plant functional types. New Phytol. 205, 973–993.
NOAA, NASA, & Air-Force, U.S, 1976. U.S. Standard Atmosphere, 1976. NOAA, U.S. Government Printing Office, Washington D.C.
Nobel, P.S., 1976. Photosynthetic rates of Sun versus shade leaves of Hyptis emoryi Torr. Plant Physiol. 58, 218–223.
North, P.R.J., 1996. Three-dimensional forest light interaction model using a Monte Carlo method. IEEE Trans. Geosci. Remote Sens. 34, 946–956.
Pacheco-Labrador, J., Perez-Priego, O., El-Madany, T.S., Julitta, T., Rossini, M., Guan, J., Moreno, G., Carvalhais, N., Martín, M.P., Gonzalez-Cascon, R., Kolle, O., Reischtein, M., van der Tol, C., Carrara, A., Martini, D., Hammer, T.W., Moossen, H., Migliavacca, M., 2019. Multiple-constraint inversion of SCOPE. Evaluating the potential of GPP and SIF for the retrieval of plant functional traits. Remote Sensing of Environment 234, 111362.
Pedrós, R., Goulas, Y., Jacquemoud, S., Louis, J., Moya, I., 2010. FluorMODleaf: a new leaf fluorescence emission model based on the PROSPECT model. Remote Sens. Environ. 114, 155–167.
Peng, B., Guan, K., Zhou, W., Jiang, C., Frankenberg, C., Sun, Y., He, L., Köhler, P., 2020. Assessing the benefit of satellite-based solar-induced chlorophyll fluorescence in crop yield prediction. Int. J. Appl. Earth Obs. Geoinf. 90, 102126.
Pradal, C., Dufour-Kowalski, S., Boudon, F., Fournier, C., Godin, C., 2008. OpenAlea: a visual programming and component-based software platform for plant modelling. Funct. Plant Biol. 35, 751–760.
Rosema, A., Verhoef, W., Schroote, J., Snel, J.F.H., 1991. Simulating fluorescence light-canopy interaction in support of laser-induced fluorescence measurements. Remote Sens. Environ. 37, 117–130.
Sakai, Y., Kobayashi, H., Kato, T., 2020. FLiES-SIF ver. 1.0: three-dimensional radiative transfer model for estimating solar induced fluorescence. Geosci. Model Dev. Discuss. 2020, 1–36.
Sloup, P., 2013. https://is.muni.cz/th/325196/fi_m/?lang=en (18 February 2020).
Sušila, P., Nauš, J., 2007. A Monte Carlo study of the chlorophyll fluorescence emission and its effect on the leaf spectral reflectance and transmittance under various conditions. Photochemical & Photobiological Sciences 6, 894–902.
Tong, C., Bao, Y., Zhao, F., Fan, C., Li, Z., Huang, Q., 2021. Evaluation of the FluorWPS model and study of the parameter sensitivity for simulating solar-induced chlorophyll fluorescence. Remote Sensing 13.
van der Tol, C., Verhoef, W., Timmermans, J., Verhoef, A., Su, Z., 2009. An integrated model of soil-canopy spectral radiances, photosynthesis, fluorescence, temperature and energy balance. Biogeosciences 6, 3109–3129.
van der Tol, C., Rossini, M., Cogliati, S., Verhoef, W., Colombo, R., Rascher, U., Mohammed, G., 2016. A model and measurement comparison of diurnal cycles of sun-induced chlorophyll fluorescence of crops. Remote Sens. Environ. 186, 663–677.
van der Tol, C., Vilfan, N., Dauwe, D., Cendrero-Mateo, M.P., Yang, P., 2019. The scattering and re-absorption of red and near-infrared chlorophyll fluorescence in the models Fluspect and SCOPE. Remote Sens. Environ. 232, 111292.
Verhoef, W., 1984. Light scattering by leaf layers with application to canopy reflectance modeling: the SAIL model. Remote Sens. Environ. 16, 125–141.
Verrelst, J., Rivera, J.P., 2017. Chapter 16 - a global sensitivity analysis toolbox to quantify drivers of vegetation Radiative transfer models. In: Petropoulos, G.P., Srivastava, P.K. (Eds.), Sensitivity Analysis in Earth Observation Modelling. Elsevier, pp. 319–339.
Verrelst, J., Schaepman, M.E., Malenovský, Z., Clevers, J.G.P.W., 2010. Effects of woody elements on simulated canopy reflectance: implications for forest chlorophyll content retrieval. Remote Sens. Environ. 114, 647–656.
Verrelst, J., Malenovský, Z., Van der Tol, C., Camps-Valls, G., Gastellu-Etchegorry, J.-P., Lewis, P., North, P., Moreno, J., 2019. Quantifying vegetation biophysical variables from imaging spectroscopy data: a review on retrieval methods. Surv. Geophys. 40, 589–629.
Verroust, A., Lazarus, F., 1999. Extracting skeletal curves from 3D scattered data. In: Proceedings Shape Modeling International '99. International Conference on Shape Modeling and Applications, pp. 194–201.
Vilfan, N., van der Tol, C., Muller, O., Rascher, U., Verhoef, W., 2016. Fluspect-B: a model for leaf fluorescence, reflectance and transmittance spectra. Remote Sens. Environ. 186, 596–615.
Vilfan, N., Van der Tol, C., Yang, P., Wyber, R., Malenovský, Z., Robinson, S.A., Verhoef, W., 2018. Extending Fluspect to simulate xanthophyll driven leaf reflectance dynamics. Remote Sens. Environ. 211, 345–356.
Vilfan, N., van der Tol, C., Verhoef, W., 2019. Estimating photosynthetic capacity from leaf reflectance and Chl fluorescence by coupling radiative transfer to a model for photosynthesis. New Phytol. 223, 487–500.
Wang, C., Guan, K., Peng, B., Chen, M., Jiang, C., Zeng, Y., Wu, G., Wang, S., Wu, J., Yang, X., Frankenberg, C., Köhler, P., Berry, J., Bernacchi, C., Zhu, K., Alden, C., Miao, G., 2020. Satellite footprint data from OCO-2 and TROPOMI reveal significant spatio-temporal and inter-vegetation type variabilities of solar-induced fluorescence yield in the U.S. Midwest. Remote Sensing of Environment *241*, 111728.
Widlowski, J.-L., Mio, C., Disney, M., Adams, J., Andredakis, I., Atzberger, C., Brennan, J., Busetto, L., Chelle, M., Ceccherini, G., Colombo, R., Côté, J.-F., Eenmäe, A., Essery, R., Gastellu-Etchegorry, J.-P., Gobron, N., Grau, E., Haverd, V., Homolová, L., Huang, H., Hunt, L., Kobayashi, H., Koetz, B., Kuusk, A., Kuusk, J., Lang, M., Lewis, P.E., Lovell, J.L., Malenovský, Z., Meroni, M., Morsdorf, F., Mõttus, M., Ni-Meister, W., Pinty, B., Rautiainen, M., Schlerf, M., Somers, B., Stuckens, J., Verstraete, M.M., Yang, W., Zhao, F., Zenone, T., 2015. The fourth phase of the radiative transfer model intercomparison (RAMI) exercise: actual canopy scenarios and conformity testing. Remote Sens. Environ. 169, 418–437.
Willmott, C.J., 1981. On the validation of models. Phys. Geogr. 2, 184–194.
Wyber, R., Malenovský, Z., Ashcroft, M., Osmond, B., Robinson, S., 2017. Do daily and seasonal trends in leaf solar induced fluorescence reflect changes in photosynthesis, growth or light exposure? Remote Sens. 9, 604.
Yang, P., van der Tol, C., 2018. Linking canopy scattering of far-red sun-induced chlorophyll fluorescence with reflectance. Remote Sens. Environ. 209, 456–467.
Yang, P., Verhoef, W., van der Tol, C., 2017. The mSCOPE model: a simple adaptation to the SCOPE model to describe reflectance, fluorescence and photosynthesis of vertically heterogeneous canopies. Remote Sens. Environ. 201, 1–11.
Yang, P., Prikaziuk, E., Verhoef, W., van der Tol, C., 2020. SCOPE 2.0: a model to simulate vegetated land surface fluxes and satellite signals. Geosci. Model Dev. Discuss. 2020a, 1–26.
Yang, P., van der Tol, C., Campbell, P.K.E., Middleton, E.M., 2020b. Fluorescence correction vegetation index (FCVI): a physically based reflectance index to separate

physiological and non-physiological information in far-red sun-induced chlorophyll fluorescence. Remote Sens. Environ. 240, 111676.
Yin, T., Gastellu-Etchegorry, J.-P., Lauret, N., Grau, E., Rubio, J., 2013. A new approach of direction discretization and oversampling for 3D anisotropic radiative transfer modeling. Remote Sens. Environ. 135, 213–223.
Zeng, Y., Badgley, G., Dechant, B., Ryu, Y., Chen, M., Berry, J.A., 2019. A practical approach for estimating the escape ratio of near-infrared solar-induced chlorophyll fluorescence. Remote Sens. Environ. 232, 111209.
Zhang, Z., Zhang, Y., Porcar-Castell, A., Joiner, J., Guanter, L., Yang, X., Migliavacca, M., Ju, W., Sun, Z., Chen, S., Martini, D., Zhang, Q., Li, Z., Cleverly, J., Wang, H., Goulas, Y., 2020. Reduction of structural impacts and distinction of photosynthetic pathways in a global estimation of GPP from space-borne solar-induced chlorophyll fluorescence. Remote Sens. Environ. 240, 111722.
Zhao, F., Dai, X., Verhoef, W., Guo, Y., van der Tol, C., Li, Y., Huang, Y., 2016. FluorWPS: a Monte Carlo ray-tracing model to compute sun-induced chlorophyll fluorescence of three-dimensional canopy. Remote Sens. Environ. 187, 385–399.